FEM-ANN approach to predict nonlinear pyro-coupled deflection of sandwich plates with agglomerated porous nanocomposite core and piezo-magneto-elastic facings in thermal environment

Vinyas Mahesh, Vishwas Mahesh & Sathiskumar A Ponnusami

Published online: 19 Apr 2023.

Submit your article to this journal ⍞

View related articles ⍞

View Crossmark data ⍞

Taylor & Francis
Taylor & Francis Group

ORIGINAL ARTICLE

OPEN ACCESS | Check for updates

FEM-ANN approach to predict nonlinear pyro-coupled deflection of sandwich plates with agglomerated porous nanocomposite core and piezo-magneto-elastic facings in thermal environment

Vinyas Mahesh[a], Vishwas Mahesh[b,c], and Sathiskumar A Ponnusami[a]

[a]Department of Engineering, City, University of London, Northampton Square, London, United Kingdom; [b]Department of Industrial Engineering and Management, Siddaganga Institute of Technology, Tumkur, Karnataka, India; [c]Department of Aerospace Engineering, Indian Institute of Science, Bangalore, Karnataka, India

ABSTRACT

The present work deals with evaluating the nonlinear deflections of the smart sandwich plate with agglomerated Carbon Nanotubes (CNTs) porous core and piezo-magneto-electric (PME) facings, using a novel finite element method (FEM) – artificial neural network (ANN) approach. For the first time, an ANN-based computational tool that integrates the effects of agglomeration of CNTs, porosity and pyro-coupling of the PME materials is presented. Firstly, an in-house finite element (FE) computational tool is proposed and developed using the principle of virtual work in association with higher-order shear deformation theory (HSDT) and von-Karman's nonlinearity. The data points owing to the nonlinear deflections are collected using the proposed FE formulation, which trains the ANN model using Levenberg–Marquardt algorithm. The externally applied thermal loads are assumed to vary uniformly and linearly across the thickness of the plate. The primary focus of this work is to assess the variation in the degree of pyro-coupling associated with agglomeration and porosity. Two states of agglomeration, such as partial and complete; three forms of porosity, such as uniformly distributed, and two variants of functionally graded porosity, are considered for investigation. Numerical examples are solved to understand the interrelated effects of these material properties. A significant variation in the deflection of the plate, which refers to its actuation capability, is witnessed when the parameters of agglomeration and porosity change.

1. Introduction

Modern-era structures demand extreme mechanical properties as they are often tested under various operating conditions. One such class of structures is the sandwich structure which usually consists of a core between the facesheets on either end. With the advancement in material technology, various forms of a core made of isotropic, functionally graded (FG), nanocomposite, porous and Carbon nanotubes (CNTs) are explored. The sandwich structures are potential candidates for aerospace, automobile, and marine structures due to the enhanced bending stiffness and lower specific weight. Recently, sandwich structures have been fabricated by introducing multifunctionality through various smart materials. Thus, their application domain is widened, ranging from energy harvesters to spacecraft structures.

Many researchers have worked on various forms of sandwich structures with different material configurations. Among them, the most relevant articles are discussed here. Quan et al. [1] proposed an analytical formulation and investigated the dynamic behavior of sandwich auxetic plates. Mota et al. [2] adopted an image-based layer-wise model and evaluated the sandwich plate's free vibration and static behavior with an aluminum core. A similar structural analysis for a functionally graded (FG) sandwich panel was performed by Gorgeri et al. [3] using a sub-laminate variable kinematic model. Koutoati et al. [4] developed a finite element (FE) model to investigate the static bending and free vibration behavior of FG sandwich beams. Hachemi [5] presented a p-version finite element approach in association with C^0 higher order shear deformation theory (HSDT) to assess the frequency response of sandwich plates with variable stiffness. Khalili et al. [6] improved the HSDT to investigate the stability characteristics of composite sandwich plates. Wu et al. [7] developed a multi-objective optimization technique to optimize the frequency response of lattice sandwich structures. Eyvazian et al. [8] proposed an unconstrained higher-order theory to investigate the dynamic characteristics of the sandwich cylinder with graphene facesheets. Setoodeh et al. [9] probed the combined effects of porous core, CNT facesheets with piezoelectric layers on the dynamic behavior of sandwich shells using the generalized differential quadrature (GDQ) method. Moradi-Dastjerdi and Behdinan [10] conducted the stability analysis of a sandwich

CONTACT Vinyas Mahesh ✉ vinyas.mahesh@gmail.com, vinyas.mahesh@city.ac.uk 🏛 Department of Engineering, City, University of London, Northampton Square, London, EC1V 0HB, United Kingdom.

plate with a porous core, graphene layers and piezoelectric face-sheets through mesh-free numerical analysis. Based on first-order shear deformation theory (FSDT) in conjunction with the mesh-free method, Moradi-Dastjerdi and Aghadavoudi [11] examined the bending performance of sandwich plates with agglomerated CNTs. Implementing modified strain gradient theory (MSGT), Arshid et al. [12] investigated the static and dynamic response of porous microplates with functionally graded graphene nanoplatelets (GNPs). Also, other prominent literature is reported on investigating the different structural behavior of porous material operated in thermal/hygrothermal environments [13–16].

A unique structural response can be expected from the interaction between the different material configurations when the sandwich structures are operated in the thermal environment. Wang et al. [17] studied the post-buckling behavior of sandwich beams with auxetic core and variant of graphene facesheets operated in the thermal environment. Xia and Shen [18] presented the effect of the thermal environment on the post-buckled vibration characteristics of sandwich plates with FG facesheets. For a thermally post-buckled sandwich beam with CNT facesheets, Mirzaei and Kiani [19] examined the snap-through behavior using the cylindrical arc-length technique. Khandelwal et al. [20] developed a FE model based on C0 higher order zigzag theory and evaluated the thermo-mechanical response of sandwich plates. The effect of arbitrary periodic load on the dynamic instability behavior of sandwich plates exposed to the thermal environment was studied by Chen et al. [21]. The comparison of the effect of various kinematic models on the bending response of FG sandwich plates exposed to thermal loading was presented by Zenkour et al. [22]. The influence of localized heating and random distribution of CNTs on the dynamic and post-buckled response of composite plates was studied by Chakraborty et al. [23] using the micromechanics approach. Karakoti et al. [24] considered porous FG sandwich panels and assessed their nonlinear transient response when subjected to blast loads in the thermal environment. Khorshidi and Karimi [25] probed the flutter behavior of sandwich plates with FG facesheets subjected to the extreme thermal environment. More insights on the effect of the thermal environment on the structural responses can be found in Refs. [26–29].

The use of smart materials in the structures can bring multifunctionality onboard and facilitate the structures to simultaneously perform different activities with the minimum expense of weight and stability. The three-field interaction of piezo-magneto-elastic (MPE)/magneto-electro-elastic (MEE) has proved to be a game-changer in various smart structure applications [30]. The multifield interaction between the various fields exhibited by MEE composites makes them a potential candidate for various engineering applications, including vibration control [31–33], energy harvesting [34–36] and impact engineering [37, 38]. Ramirez et al. [39] investigated the natural frequencies of MEE plates under the framework of the discrete layer model. Based on the meshless method, the deflections of circular MEE plates were determined by Sladek et al. [40]. Davi et al. [41] employed the boundary element method and investigated

the static performance of bimorph beams in detail. Mahesh et al. [42] studied the effect of topological texture associated with the auxeticity on the frequency response of MEE sandwich plates using the FE approach. Quang et al. [43] presented an analytical model to assess the static buckling of MEE sandwich structure subjected to multi-physics loads. Dat et al. [44] probed the effect of blast loads on the dynamic behavior of MEE plates with auxetic cores. Nie et al. [45] developed a stable node-based smoothed radial point interpolation method to examine the dynamic response of MEE structures. The influence of multi-physics loading on the nonlinear deflections of MEE structures with CNTs reinforcement [46] and porosity [47] has also been reported in the literature. A similar analysis but for MEE cylindrical shells was performed by Zhao et al. [48]. Ewolo Ngak et al. [49] probed on the static behavior of MEE structures with the help of the state-space approach. Akbarzadeh and Chen [50] developed analytical solutions to determine the effect of thermos-mechanical loads on the stress distribution in an MEE cylinder. Arshid et al. [51] probed the vibration characteristics of FG-GNP shells with MPE layers exposed to hygrothermal fields using HSDT. Khorsani et al. [52] carried out a similar analysis for the plate configuration. Similarly, Amir et al. [53, 54] studied the vibration characteristics of porous/MPE sandwich rectangular/annular plates subjected to pre-loads using second-order shear deformation theory (SSDT). The influence of magnetostrictive layers on the vibration behavior of a circular sandwich plate with a magnetorheological core exposed to a magnetic field was studied by Amir et al. [55]. The above-discussed literature highlights that the degree of computational accuracy of any structural response is directly dependent on the kinematic displacement model (KDM) assumed for the analysis. Hence, it is important to choose the apt KDM [56, 57].

Due to the multifield interactive capability of the MEE composites, it exhibits thermo-electric and thermo-magnetic coupling when operated in the thermal environment. These are termed 'pyro-coupling' effects. Several kinds of research were reported on the thermal analysis of smart MEE structures, but a few focus on the pyro-coupling effects on the structural responses. Vinyas and Kattimani [58, 59] showed that pyro-coupling enhances the multifunctionality of the stepped functionally graded MEE beams and plates. In addition, Vinyas and his group conducted several pilot studies on various structural responses of MEE composites operated in the thermal environment highlighting the influence of pyro-coupling [60–62].

As the complexity of the structure and/or its operating conditions enhances, it becomes difficult for the conventional techniques to deal with the large database. Therefore, there exists a necessity for a powerful tool to overcome these hurdles without compromising the accuracy of the analysis. Artificial neural network (ANN) is one such approach which is well embraced by the research community [63]. By using the preliminary dataset, ANN can develop realistic predictive models. Several researchers have worked on predicting structural responses based on ANN. The frequency behavior
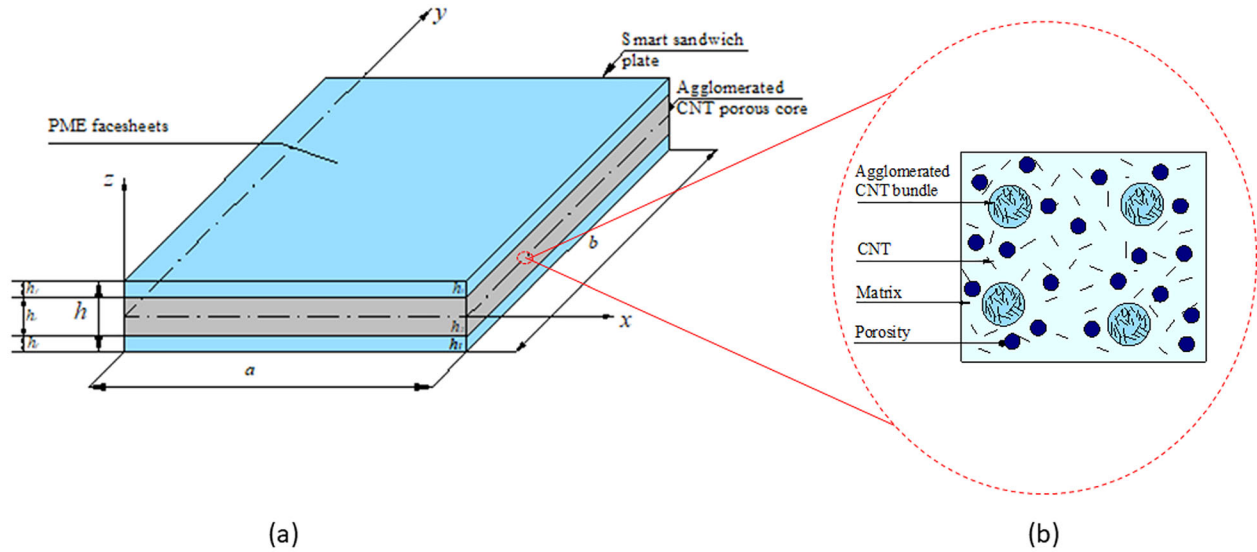
Figure 1. Geometric representation of (a) APC/PME sandwich plate (b) RVE of agglomerated CNT porous core.

of porous functionally graded plates following higher-order shear deformation theory was predicted using ANN by Rjoub and Alshatnawi [64]. Atilla et al. [65] investigated composite plate vibration and stability response using ANN. Kallanavar et al. [66] proposed an ANN model to predict the influence of temperature and moisture on the frequencies of layered composite plates.

The literature review showed that limited works had been reported assessing porous PME structures' coupled response. Moreover, to the best of the author's knowledge, this is the first work in the open literature that collectively models the CNT agglomeration, porosity, and pyro-coupled interactions and investigates their effects on the actuation capabilities of smart sandwich structures. In addition, this article also exploits the advantages of artificial neural network (ANN) for predicting the nonlinear deflections of the smart sandwich PME structures, which is the first of its kind. The FEM-ANN approach can reduce the higher computational costs of investigating complex multifunctional structures via other numerical approaches. Also, it provides flexibility to assess irregular structures, which is difficult through other conventional/analytical methods previously reported. The complexity of the assessment and in-depth understanding of the synergistic effects makes the work interesting. The outcomes of this work can be directly applied to aviation, soft robotics, and vibration control applications.

2. Problem description

In this research, a smart sandwich plate (SSP) made of agglomerated CNT core with pores (APC) and PME material facings subjected to different temperature profiles have been considered for evaluation. The schematic of the plate is shown in Figure 1(a), where side length, width, overall thickness, core thickness and facesheet thickness are represented by a, b, h, h_c and h_{fs}, respectively. The material

properties of PME facings and polymer core are depicted in Tables 1 and 2, respectively.

The details of the temperature profiles and their corresponding mathematical expressions can be written as,

(a) Uniform temperature rise (UTR): $T(z) = \Delta T = 300$
(b) Linear temperature rise (LTR) with two variants. First, the highest and lowest temperatures appear at the top (T_{ts}) and bottom (T_{bs}) facesheets, respectively. Another is the vice-versa. From here onwards, they are designated LTR (HT-LB) and LTR (LT-HB). The mathematical expression is [58]

$$T(z) = (T_{ts} - T_{bs})\left\{\frac{z}{h} + \frac{1}{2}\right\} + T_{bs} \tag{1}$$

Further, for LTR (HT-LB): $T_{ts} = 400K$ and $T_{bs} = 300K$, whereas for LTR (LT-HB): $T_{ts} = 300K$ and $T_{bs} = 400K$.

3. Materials and methods

The two-parameter micromechanics model developed based on Eshelby-Mori-Tanaka (EMT) equations are enforced on the representative volume element (RVE) [67]. The RVE of the agglomerated CNT core is shown in Figure 1(b). It can be shown that

$$V^r = V^r_{incl} + V^r_m \tag{2}$$

where V^r, V^r_m and V^r_{incl} are the CNT volume fraction inside RVE, matrix and CNT volume fraction inside the agglomeration, respectively.

The indicators μ and η are defined to specify the agglomeration states as follows [66]:

$$\mu = \frac{V_{incl}}{V}; \eta = \frac{V^r_{incl}}{V^r}; f_r = \frac{V^r}{V} \tag{3}$$

Considering the inside and outside the region of the agglomeration, the shear (K_{in}, K_{out}) and bulk moduli (G_{in},

Table 1. Coupled properties of multiphase MEE (50% BaTiO$_3$-50% CoFe$_2$O$_4$ composite) [58].

Material property	Material constants	0.5 V_f (50% PE+ 50% PM)
Elastic constants (GPa)	$C_{11} = C_{22}$	220
	C_{12}	120
	$C_{13} = C_{23}$	120
	C_{33}	215
	$C_{44} = C_{55}$	45
	C_{66}	50
Piezoelectric constants (C/m^2)	$e_{31} = e_{32}$	−3.5
	e_{33}	9.0
	$e_{15} = e_{24}$	0
Dielectric constant (10^{-9} C^2/Nm^2)	$\eta_{11} = \eta_{22}$	0.85
	η_{33}	6.3
Magnetic permeability (10^{-4} Ns^2/C^2)	$\mu_{11} = \mu_{22}$	−2.0
	μ_{33}	0.9
Piezomagnetic constants (N/Am)	$q_{31} = q_{32}$	350
	q_{33}	320
	$q_{15} = q_{24}$	200
Magneto-electric constant (10^{-12}Ns/VC)	$m_{11} = m_{22}$	5.5
	m_{33}	2600
Pyroelectric-constant (10^{-7} C/m^{2}K)	p_2	−7.8
Pyromagnetic constant (10^{-5} C/m^{2}K)	τ_2	−23
Thermal expansion coefficient (10^{-6}K^{-1})	$\alpha_1 = \alpha_2$	12.3
	α_3	8.2
Density (kg/m^3)	ρ	5550

Table 2. Material properties of polymer material and CNT [27].

Material property	PMMA	CNT
Elastic modulus (GPa)	$E^m = 2.5$	$E_{11}^{CNT} = 5646.6$; $E_{22}^{CNT} = 7080$
Density (kg/m^3)	$\rho_m = 1150$	$\rho_{CNT} = 1400$
Poisson's ratio	$\nu^m = 0.34$	$\nu_{CNT} = 0.175$

G_{out}) can be expressed in terms of the matrix's shear (K_m) and bulk (G_m) moduli as [67]:

$$K_{in} = K_m + \frac{(\delta_r - 3K_m\alpha_r)f_r\eta}{3(\mu - f_r\eta(1-\alpha_r))}$$
$$K_{out} = K_m + \frac{(\delta_r - 3K_m\alpha_r)f_r(1-\eta)}{3[1 - \mu - f(1-\eta) + (1-\eta)f_r\alpha_r]}$$
$$G_{in} = G_m + \frac{(\eta_r - 3G_m\beta_r)f_r\eta}{2(\mu - f_r\eta(1-\beta_r))}$$
$$G_{out} = G_m + \frac{(\eta_r - 2G_m\beta_r)f_r(1-\eta)}{2[1 - \mu - f_r(1-\eta) + f_r(1-\eta)\beta_r]}$$
(4)

The various terms used in Eq. (4) are expressed as,

$$\alpha_r = \frac{k_r - l_r + 3(K_m + G_m)}{3(K_m + k_r)}$$
$$\beta_r = \frac{1}{5}\left\{\frac{4G_m + 2k_r + l_r}{3(G_m + k_r)} + \frac{4G_m}{G_m + p_r}\right.$$
$$\left. + \frac{2[G_m(3K_m + G_m) + G_m(3K_m + 7G_m)]}{G_m(3K_m + G_m) + m_r(3K_m + 7G_m)}\right\}$$
$$\delta_r = \frac{1}{3}\left[\eta_r + 2l_r + \frac{(2k_r + l_r)(3K_m + G_m - l_r)}{G_m + k_r}\right]$$
$$\eta_r = \frac{1}{5}\left[\frac{2}{3}(\eta_r - l_r) + \frac{8G_m p_r}{G_m + p_r} + \frac{8m_r G_m(3K_m + 4G_m)}{3K_m(G_m + p_r) + G_m(7m_r + G_m)}\right.$$
$$\left. + \frac{2(k_r - l_r)(2G_m + l_r)}{3(G_m + k_r)}\right]$$
(5)

Table 3. Different parameters and their ranges selected for the development of ANN model.

Sl. No	Parameters	Range
1	PME volume fraction (V_f)	50%, 80%
2	Temperature profiles	UTR, HT-LB, LT-HB
3	Core material	Pure polymer, porous core, CNT-NCC
4	Porosity volume (λ_o)	0.2, 0.4, 0.6, 0.8
5	Porosity pattern	UD, FG-NS, FG-S
6	Boundary condition	CCCC, SSSS, CFCF, CSCS
7	CNT volume fraction (f_r)	1%, 2% and 3%
8	μ	0.25, 0.5, 0.75, 1.0
9	η	1.0, 0.75, 0.45, 0.25

Using Eqs. (4) and (5), the effective bulk (K) and shear moduli (G) of the overall composite can be written as [67]:

$$K = K_{out}\left[1 + \frac{\mu\left(\frac{K_{in}}{K_{out}} - 1\right)}{1 + \alpha(1-\mu)\left(\frac{K_{in}}{K_{out}} - 1\right)}\right];$$
$$G = G_{out}\left[1 + \frac{\mu\left(\frac{G_{in}}{G_{out}} - 1\right)}{1 + \beta(1-\mu)\left(\frac{G_{in}}{G_{out}} - 1\right)}\right]$$

here,

$$\nu_{out} = \frac{(3K_{out} - 2G_{out})}{2(3K_{out} + 2G_{out})}; \alpha = \frac{1 + \nu_{out}}{3(1 - \nu_{out})}; \beta = \frac{2(4 - 5\nu_{out})}{15(1 - \nu_{out})}$$
(6)

The effective Elastic modulus (E) and Poisson's ratio (ν) of the nanocomposite considering agglomeration can be shown as:

$$E = \frac{9KG}{3K + G}; \nu = \frac{3K - 2G}{6K + 2G}$$
(7)

The effective mass density (ρ) calculated according to Voigt's rule is shown as follows:

$$\rho = f_r\rho_r + f_m\rho_m$$
(8)

where f_r and f_m are the CNT and matrix volume fractions, and the ρ_r and ρ_m are the corresponding densities. In addition, the thermal expansion coefficient (α) of the agglomerated CNT nanocomposite core is represented as [68]

$$\alpha = \frac{[E + 4\nu(1+\nu)K]\alpha_{11} + 4(1+\nu)K\alpha_{22}}{E + 4(1+\nu)^2 K}$$
(9)

in which,

$$\alpha_{11} = \frac{f_r E_{11}^{CNT}\alpha_{11}^{CNT} + f_m E_m\alpha_m}{f_r E_{11}^{CNT} + f_m E_m}$$
$$\alpha_{22} = (1 + \nu_{CNT})f_r\alpha_{22}^{CNT} + (1 + \nu_m)f_r\alpha_m - \nu\alpha_{11}$$
(10)

Meanwhile, this article considers three forms of porosity distributions: uniformly distributed (UD), symmetric and asymmetric functional graded denoted by FG-S and FG-NS. The mathematical expressions of the agglomerated CNT porous core's Young's modulus (E^c) and density (ρ^c) owing to these distributions are shown as [69],
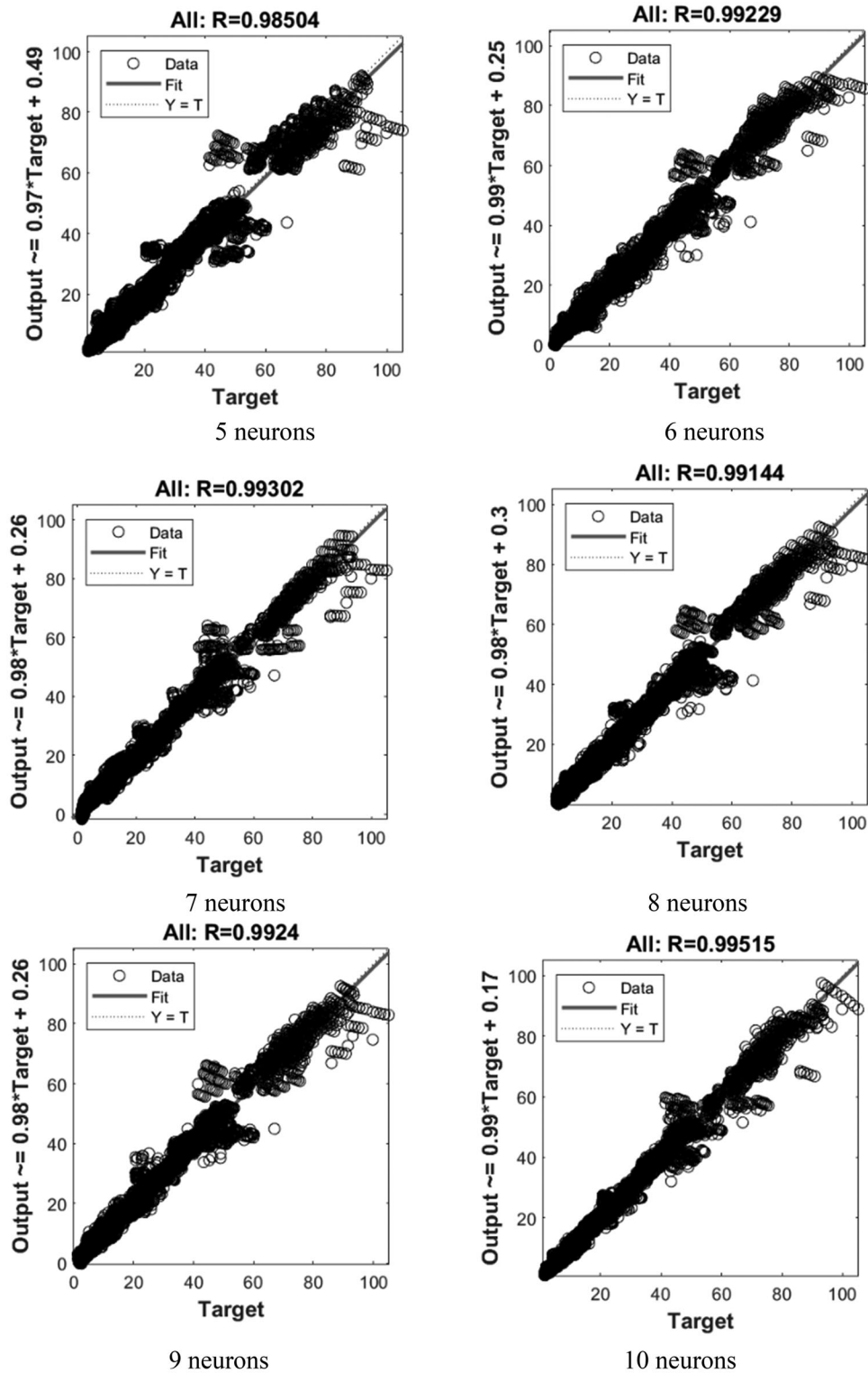
(a)

Figure 2. The schematic of (a) regression plots with different number of neurons (b) regression plots for training, validation test and overall performance of the optimum ANN model with ten neurons.
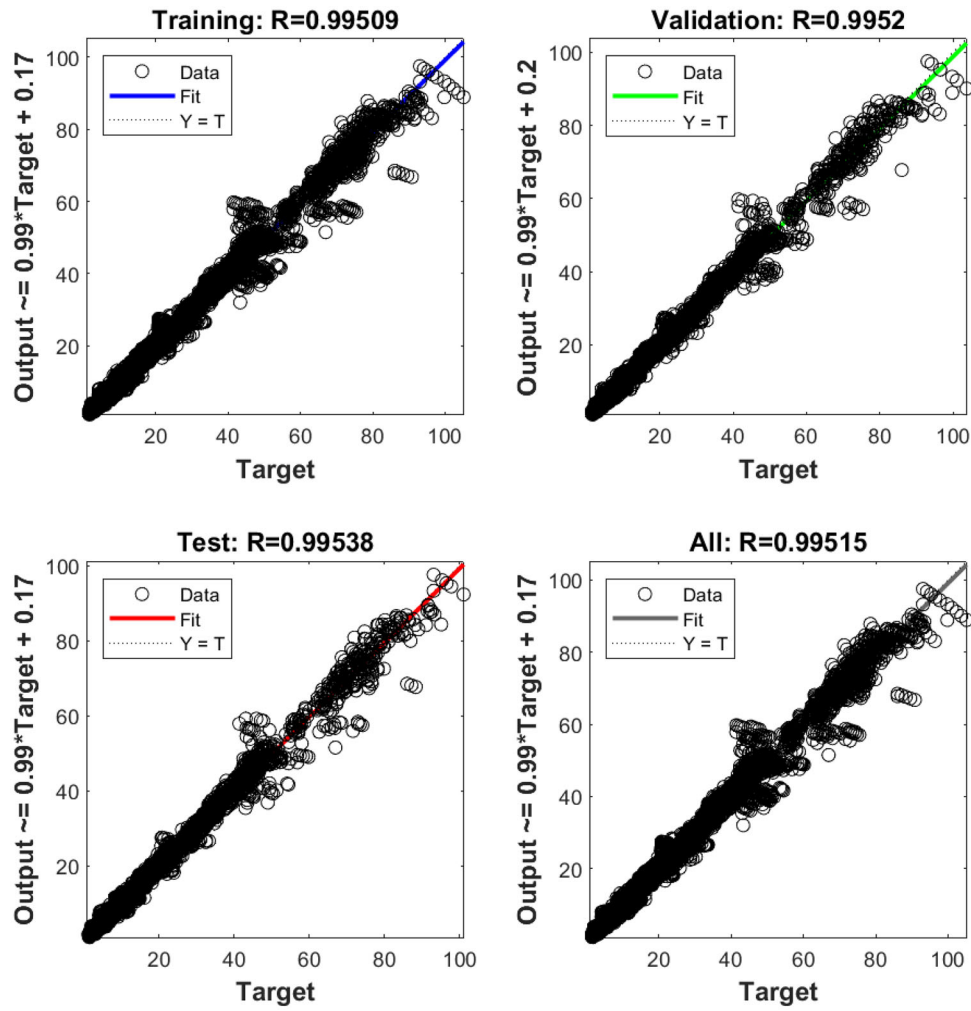
Figure 2. Continued.

$$FG\text{-}S : E^c = (1 - \lambda_o \cos(\pi z/h_c))E;$$

$$\rho^c = \left(1 - \left(1 - \sqrt{1 - \lambda_o}\right)\cos(\pi z/h_c)\right)\rho$$

$$FG\text{-}NS : E^c = \left(1 - \lambda_o \cos\left(\pi z/2h_c + \pi/4\right)\right)E;$$

$$\rho^c = \left(1 - \left(1 - \sqrt{1 - \lambda_o}\right)\cos\left(\pi z/2h_c + \pi/4\right)\right)\rho \quad (11)$$

$$UD : E^c = \left(\frac{2}{\pi}\sqrt{1 - \lambda_o} - \frac{2}{\pi} + 1\right)^2 E;$$

$$\rho^c = \left(\frac{2}{\pi}\sqrt{1 - \lambda_o} - \frac{2}{\pi} + 1\right)^2 \rho$$

here, λ_o is the porosity volume, and E is Young's modulus of agglomerated CNT. Further, the Poisson's ratio of the core (ν^c) can be written as [69],

$$\nu^c = 0.221\left(1 - \frac{\rho^c}{\rho}\right)$$

$$+ \nu\left(0.342\left(1 - \frac{\rho^c}{\rho}\right)^2 - 1.21\left(1 - \frac{\rho^c}{\rho}\right) + 1\right) \quad (12)$$

Table 4. Verification of fundamental natural frequencies of completely agglomerated plates ($a/b = 1$; $a/h = 50$; CCCC).

CNT distribution	$\eta = 1.00; \mu = 0.25$		$\eta = 1.00; \mu = 0.5$		$\eta = 1.00; \mu = 0.75$	
	Craveiro and Loja [72]	Present	Craveiro and Loja [72]	Present	Craveiro and Loja [72]	Present
UD	7.2119	7.2011	9.8010	9.7893	8.5212	8.4438
FG-S	7.2801	7.2573	10.6382	10.4593	8.8357	8.8033
FG-NS	6.9518	6.9321	7.9533	7.9434	8.9882	8.9454

It is worth mentioning that the agglomerated CNT porous core's thermal expansion coefficient varies similarly to that of E^c.

The interaction between the magnetic, electric and elastic phases of the multifunctional PME facesheets can be represented through the coupled constitutive equations as follows [58]:

$$\{\sigma\} = [Q]\{\varepsilon\} - [e]\{E\} - [q]\{H\} - [Q][\alpha]\Delta T$$

$$\{D\} = [e]^T\{\varepsilon\} + [\eta]\{E\} + [m]\{H\} + [p]\Delta T \quad (13)$$

$$\{B\} = [q]^T\{\varepsilon\} + [m]\{E\} + [\mu]\{H\} + [\tau]\Delta T$$

The matrix [Q] encapsulates the coupled elastic coefficients, [e] and [q] denote the matrix of piezoelectric and

magnetostrictive coefficients. Similarly, $[m]$, $[\eta]$, and $[\mu]$ show the matrices of electromagnetic, dielectric and magnetic permeability coefficients. The pyro-electric and pyromagnetic coefficients are denoted by $[p]$ and $[\tau]$. The terms on the LHS of Eq. (13) are the stress vector $\{\sigma\}$, the electric displacement vector $\{D\}$ and the magnetic flux vector $\{B\}$.

3.1. Displacement model

The sandwich plate kinematics is governed by the HSDT, whose displacements in the *x, y,* and *z* axes are as follows [70]:

$$u = u_0 + z\theta_x - \frac{4}{3h^2}z^3\left(\theta_x + \frac{\partial w_0}{\partial x}\right)$$

$$v = v_0 + z\theta_y - \frac{4}{3h^2}z^3\left(\theta_y + \frac{\partial w_0}{\partial y}\right) \quad (14)$$

$$w = w_0$$

3.2. Nonlinear strain-displacement relation

The following is the nonlinear relation between the strains (bending $\{\varepsilon_b\}$ and shear $\{\varepsilon_s\}$ strains) and displacements [60]:

$$\{\varepsilon_b\} = \begin{Bmatrix} \varepsilon_x \\ \varepsilon_y \\ \gamma_{xy} \end{Bmatrix} = \begin{Bmatrix} \frac{\partial u_o}{\partial x} + \frac{1}{2}\left(\frac{\partial w_o}{\partial x}\right)^2 \\ \frac{\partial v_o}{\partial y} + \frac{1}{2}\left(\frac{\partial w_o}{\partial y}\right)^2 \\ \frac{\partial u_o}{\partial y} + \frac{\partial v_o}{\partial x} + \frac{\partial w_o}{\partial x}\cdot\frac{\partial w_o}{\partial y} \end{Bmatrix}$$

$$+ z\begin{Bmatrix} \frac{\partial \theta_x}{\partial x} \\ \frac{\partial \theta_y}{\partial y} \\ \frac{\partial \theta_x}{\partial y} + \frac{\partial \theta_y}{\partial x} \end{Bmatrix} - \frac{4z^3}{3h^2}\begin{Bmatrix} \frac{\partial \theta_x}{\partial x} + \frac{\partial^2 w_o}{\partial x^2} \\ \frac{\partial \theta_y}{\partial y} + \frac{\partial^2 w_o}{\partial y^2} \\ \frac{\partial \theta_x}{\partial y} + \frac{\partial \theta_y}{\partial x} + 2\frac{\partial^2 w_o}{\partial x \partial y} \end{Bmatrix}$$

$$(15)$$

$$\{\varepsilon_s\} = \begin{Bmatrix} \gamma_{xz} \\ \gamma_{yz} \end{Bmatrix} = \begin{Bmatrix} \theta_x + \frac{\partial w_o}{\partial x} \\ \theta_y + \frac{\partial w_o}{\partial y} \end{Bmatrix} - \frac{4z^2}{h^2}\begin{Bmatrix} \theta_x + \frac{\partial w_o}{\partial x} \\ \theta_y + \frac{\partial w_o}{\partial y} \end{Bmatrix} \quad (16)$$
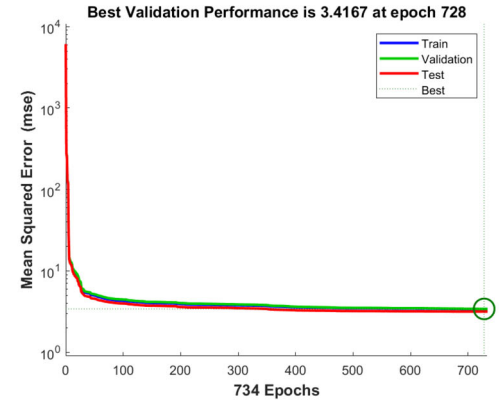
3.3. Finite element formulation

The eight-noded isoparametric element with nine degrees of freedom at each node is used to discretise the sandwich plates. They are grouped into displacement and potentials, with designations like $\{s_t\}$, $\{s_r\}$, $\{s_{r*}\}$, ψ and ϕ. They can also be expressed using shape functions, such as [61]

$$\{s_t\} = [N_t]\{s_t^e\}; \ \{s_r\} = [N_r]\{s_r^e\}; \ \{s_{r*}\} = [N_{r*}]\{s_{r*}^e\}$$

$$\phi = [N_\phi]\{\phi^e\}; \ \psi = [N_\psi]\{\psi^e\}$$

$$(17)$$

in which,
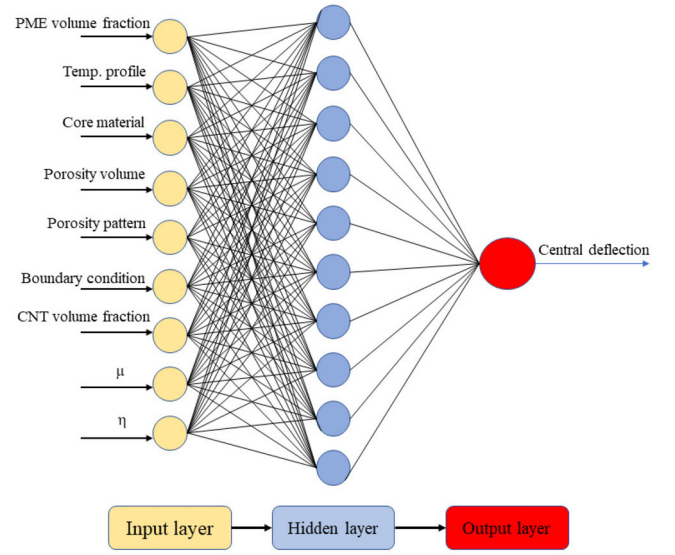
(a)

(b)

(c)

Figure 3. The (a) architecture (b) performance (c) error histogram of the final optimum ANN model trained to predict the central deflections of APC/PME sandwich plate.

$$\{s_t^e\} = \begin{bmatrix} \{s_{t1}^e\}^T & \{s_{t2}^e\}^T & \cdots\{s_{t8}^e\}^T \end{bmatrix}^T,$$

$$\{s_r^e\} = \begin{bmatrix} \{s_{r1}^e\}^T & \{s_{r2}^e\}^T & \cdots\{s_{r8}^e\}^T \end{bmatrix}^T \quad (18)$$

$$\{s_{r*}^e\} = \begin{bmatrix} \{s_{r*1}^e\}^T & \{s_{r*2}^e\}^T & \cdots\{s_{r*8}^e\}^T \end{bmatrix}^T$$
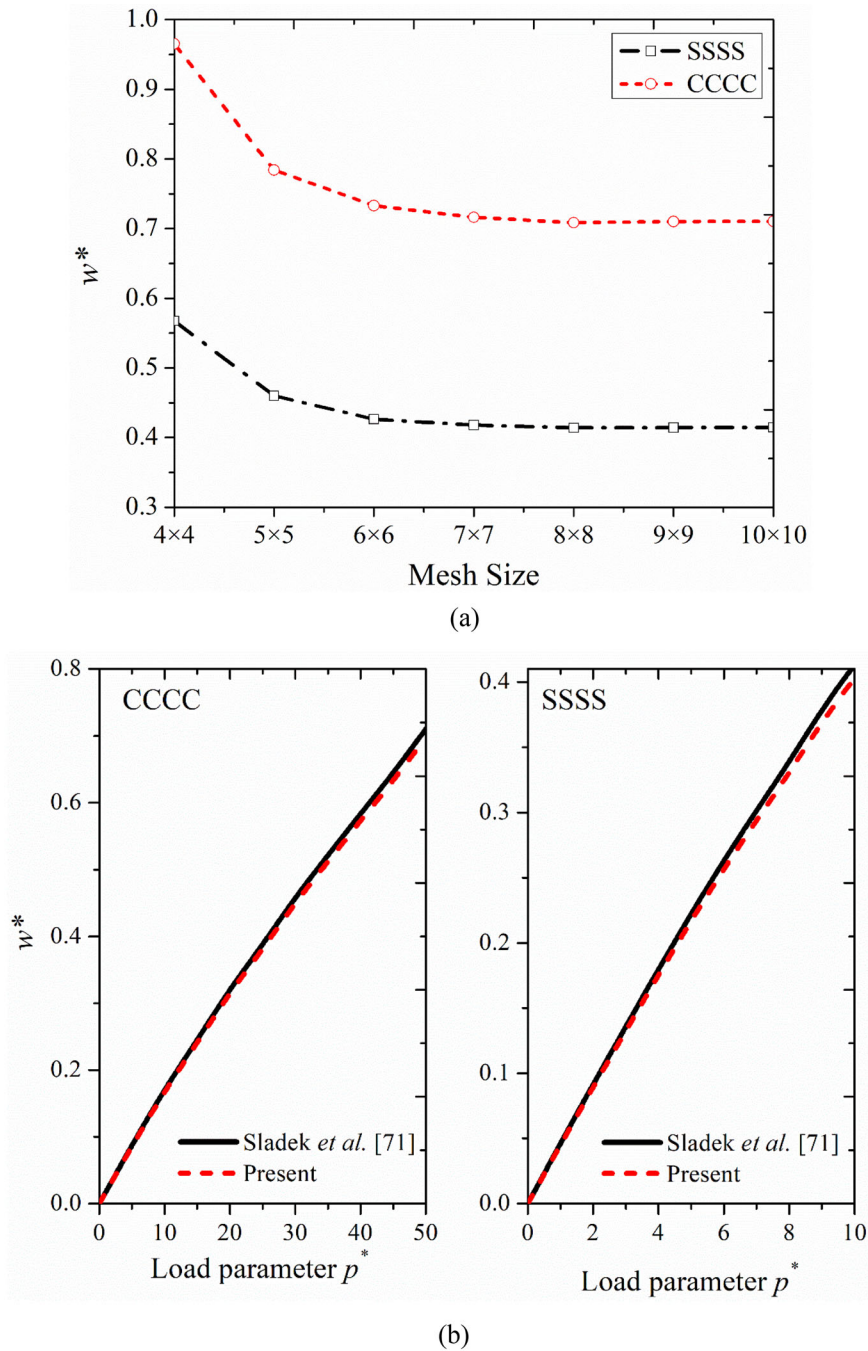
Figure 4. The (a) convergence (b) verification of the proposed FE formulation for deflection of PME plates with clamped and simply supported boundary conditions.

and

$$\{s_{ti}\} = \begin{bmatrix} u_{0i} & v_{0i} & w_{0i} \end{bmatrix}^T, \quad \{s_{ri}\} = \begin{bmatrix} \theta_{xi}\theta_{yi} \end{bmatrix}^T,$$
$$\{s_{r*i}\} = \begin{bmatrix} \kappa_{xi}\kappa_{yi} \end{bmatrix}^T \ (i = 1, 2, 3...8) \tag{19}$$

The components of the bending strain of Eq. (15) include linear and nonlinear strains as follows [41]:

$$\{\varepsilon_b\} = \{\varepsilon_{b\_L}\} + \{\varepsilon_{b\_NL}\} \tag{20}$$

In terms of FE quantities, the strains can be expressed as

$$\{\varepsilon_{b\_L}\} = [SD_{tb}]\{s_t\} + z[SD_{rb}]\{s_r\} + c_1 z^3 [SD_{rb}]\{s_r\}$$
$$+ c_1 z^3 [SD_{rb}]\{s_{r*}\}$$

$$\{\varepsilon_{b\_NL}\} = \frac{1}{2}[SD_1][SD_2]\{s_t\} \tag{21}$$

Therefore, Eq. (21) can be re-written as follows:

$$\{\varepsilon_b\} = [SD_{tb}]\{s_t\} + z[SD_{rb}]\{s_r\} + c_1 z^3 [SD_{rb}]\{s_r\}$$
$$+ c_1 z^3 [SD_{rb}]\{s_{r*}\} + \frac{1}{2}[SD_1][SD_2]\{s_t\} \tag{22}$$
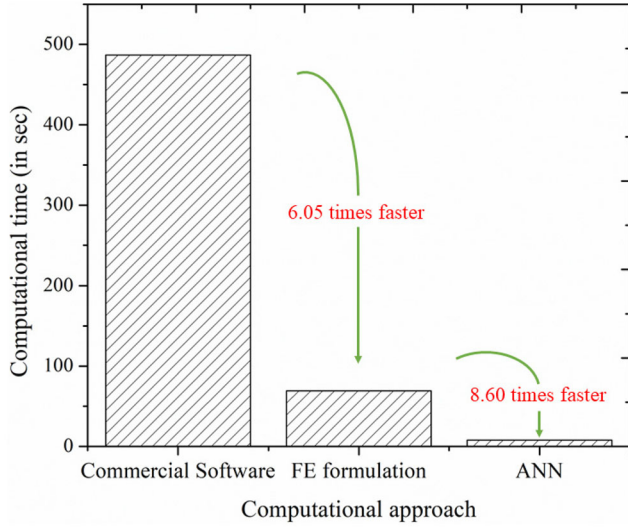
Figure 5. Computational efficiency of the proposed FE formulation and trained ANN model to assess the deflection of APC/PME sandwich plate.

Similarly, the shear strains can be expressed as

$$\{\varepsilon_s\} = [SD_{ts}]\{s_t\} + [SD_{rs}]\{s_r\} + c_2 z^2 [SD_{rs}]\{s_r\}$$
$$+ c_2 z^2 [SD_{rs}]\{s_{r*}\} \quad (23)$$

The electric and magnetic fields throughout the thickness of the PME facesheets may be represented using Maxwell's equation as follows, depending on the variation of the potentials considered. as follows [60]:

$$\{E\} = \begin{Bmatrix} E_x^u \\ E_y^u \\ E_z^u \end{Bmatrix} + \begin{Bmatrix} E_x^l \\ E_y^l \\ E_z^l \end{Bmatrix} = \begin{Bmatrix} -\frac{\partial \phi^u}{\partial x} \\ -\frac{\partial \phi^u}{\partial y} \\ -\frac{\partial \phi^u}{\partial z} \end{Bmatrix} + \begin{Bmatrix} -\frac{\partial \phi^l}{\partial x} \\ -\frac{\partial \phi^l}{\partial y} \\ -\frac{\partial \phi^l}{\partial z} \end{Bmatrix}$$

$$\{H\} = \begin{Bmatrix} H_x^u \\ H_y^u \\ H_z^u \end{Bmatrix} + \begin{Bmatrix} H_x^l \\ H_y^l \\ H_z^l \end{Bmatrix} = \begin{Bmatrix} -\frac{\partial \psi^u}{\partial x} \\ -\frac{\partial \psi^u}{\partial y} \\ -\frac{\partial \psi^u}{\partial z} \end{Bmatrix} + \begin{Bmatrix} -\frac{\partial \psi^l}{\partial x} \\ -\frac{\partial \psi^l}{\partial y} \\ -\frac{\partial \psi^l}{\partial z} \end{Bmatrix}$$

$$(24)$$

in terms of FE parameters, it can be written as

$$E = -[Z_t][SD_\phi]\{\phi^e\} - [Z_b][SD_\phi]\{\phi^e\}$$
$$H = -[Z_t][SD_\psi]\{\psi^e\} - [Z_b][SD_\psi]\{\psi^e\} \quad (25)$$

where

$$[Z_t] = \frac{1}{h}\begin{bmatrix} 0 & 0 & 0 \\ 0 & 0 & 0 \\ 0 & 0 & z-h_3 \end{bmatrix}; [Z_b] = \frac{1}{h}\begin{bmatrix} 0 & 0 & 0 \\ 0 & 0 & 0 \\ 0 & 0 & h_2-z \end{bmatrix} \quad (26)$$

3.4. The total potential energy principle

The total potential energy for the sandwich plate with porous agglomerated CNT core and PME skins can be written as follows [60]:
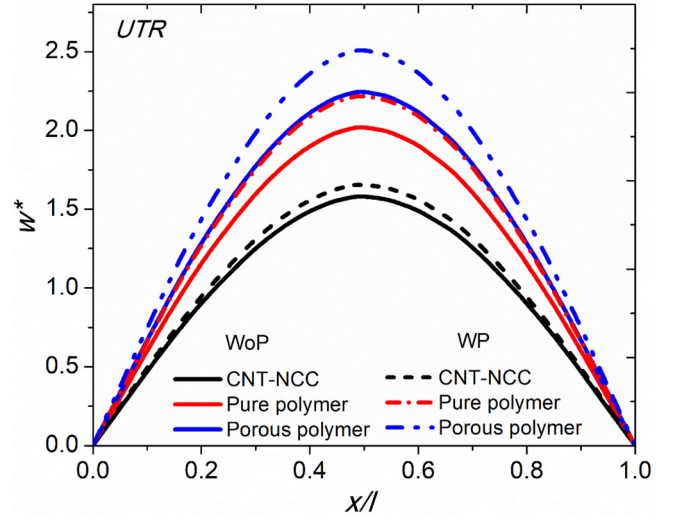

Figure 6. Influence of core material on the deflection of APC/PME sandwich plate subjected to uniform thermal environment ($a/b = 1$; $a/h = 50$; CCCC; UTR; $f_r = 2\%$; $\lambda_o = 0.8$; $V_f = 50\%$).

Table 5. Effect of plate's core material subjected to different temperature profiles predicted by in-house developed FEM and ANN tools ($a/b = 1$; $a/h = 50$; CCCC; $f_r = 2\%$).

Temperature profiles	Porous core (FG-S; $\lambda_o = 0.8$)			Polymer core			CNT-NCC		
	FEM	ANN	Error%	FEM	ANN	Error%	FEM	ANN	Error%
UTR	2.51	2.47	1.59	2.22	2.17	2.25	1.73	1.68	2.54
HT-LB	4.40	4.32	1.84	3.25	3.18	2.12	1.80	1.76	2.18
LT-HB	1.91	1.88	1.35	1.84	1.80	2.34	1.65	1.61	2.62

$$\delta T_p = \sum_{N=1}^{3} \left[\frac{1}{2}\int_{\Omega^N} \delta\{\varepsilon_b\}^T\{\sigma_b\}d\Omega^N + \frac{1}{2}\int_{\Omega} \delta\{\varepsilon_s\}^T\{\sigma_s\}d\Omega^N \right.$$
$$-\frac{1}{2}\int_{\Omega^N} \delta\{E\}^T\{D\}d\Omega^N$$
$$\left. -\frac{1}{2}\int_{\Omega^N} \delta\{H\}^T\{B\}d\Omega^N \right] - \int_A \phi Q^\phi dA - \int_A \psi Q^\psi dA = 0$$
$$(27)$$

Replacing the terms of Eq. (27) with the constitutive equations (Eq. (13)) and FE entities (Eqs. (17–26)) and further condensing based on the degrees of freedom as shown in Appendix A, the equations of motion can be written as follows [60]:

$$([S_1] + [S_{NL1}])\{s_t\} + ([S_2] + [S_{NL2}])\{s_r\}$$
$$+ ([S_3] + [K_{NL3}])\{s_{r*}\} + ([S_4] + [S_{NL4}])\{\phi\} \quad (28.\ a)$$
$$+ ([S_5] + [S_{NL5}])\{\psi\} = \{F_T\}$$

$$([S_6] + [S_{NL6}])\{s_t\} + [S_7]\{s_r\} + [S_8]\{s_{r*}\}$$
$$+ [S_9]\{\phi\} + [S_{10}]\{\psi\} = 0 \quad (28.\ b)$$

$$([S_{11}] + [S_{NL7}])\{s_t\} + [S_{12}]\{s_r\} + [S_{13}]\{s_{r*}\}$$
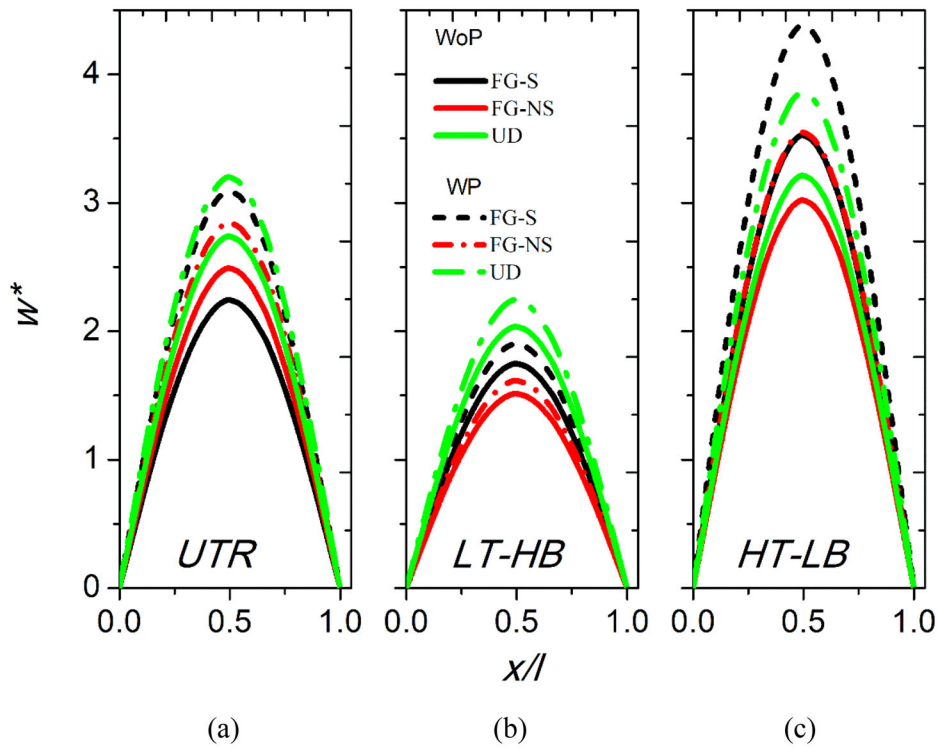$$+ [S_{14}]\{\phi\} + [S_{15}]\{\psi\} = 0 \quad (28.\ c)$$

Figure 7. Influence of porosity pattern on the deflection of APC/PME sandwich plate with porous core subjected to (a) UTR (b) LTHB (c) HT-LB temperature profiles (a/b = 1; a/h = 50; CCCC; $\lambda_o = 0.8$).

Table 6. Effect of porosity pattern and different temperature profiles on the central deflection of plate as predicted by in-house developed FEM and ANN tools ($\lambda_o = 0.8$; a/b = 1; a/h = 50; CCCC).

Porosity Patterns	UTR			HT-LB			LT-HB		
	FEM	ANN	Error%	FEM	ANN	Error%	FEM	ANN	Error%
UD	3.20	3.11	2.74	3.86	3.76	2.57	2.25	2.21	1.65
FG-NS	2.85	2.79	2.12	3.55	3.48	1.96	1.62	1.58	2.06
FG-S	2.51	2.47	1.59	4.40	4.32	1.84	1.91	1.88	1.35

Table 7. Effect of porosity volume and different temperature profiles on the central deflection of plate as predicted by in-house developed FEM and ANN tools (UD porosity; a/b = 1; a/h = 50; CCCC).

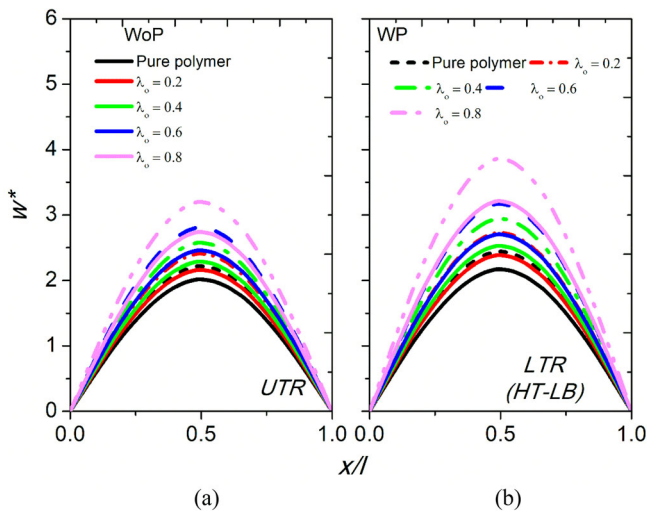| Temperature profiles	$\lambda o = 0.2$			$\lambda o = 0.4$			$\lambda o = 0.8$		
	FEM	ANN	Error%	FEM	ANN	Error%	FEM	ANN	Error%
UTR	2.41	2.38	1.17	2.58	2.55	1.12	3.20	3.11	2.74
HT-LB	2.64	2.60	1.19	2.95	2.911	1.32	3.86	3.76	2.57
LT-HB	1.94	1.92	1.04	2.18	2.15	1.24	2.25	2.21	1.65

Figure 8. Influence of porosity volume on the deflection of APC/PME sandwich plate with pure porous core subjected to (a) UTR (b) HT-LB.
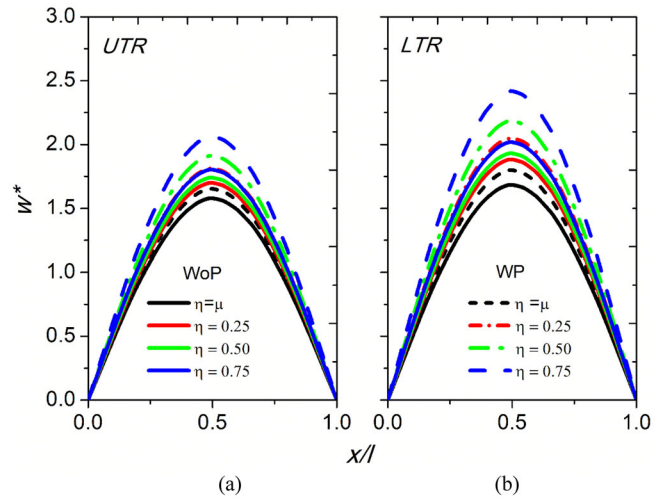

Figure 9. Influence of the parameter η on the deflection of APC/PME sandwich plate with partial agglomerated CNT nanocomposite core without pores (a/b = 1; a/h = 50; CCCC; f_r = 2%).

Figure 10. Influence of the parameter μ on the deflection of APC/PME sandwich plate with complete agglomerated CNT nanocomposite core without pores ($a/b = 1$; $a/h = 50$; CCCC; $f_r = 2\%$).
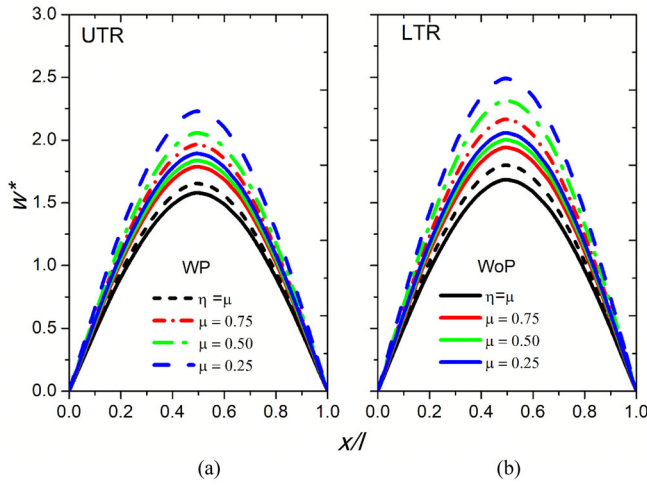
Table 8. Effect of partial agglomeration state ($\mu = 0.50$) and different temperature profiles on the central deflection of plate as predicted by in-house developed FEM and ANN tools ($a/b = 1$; $a/h = 50$; CCCC).

Temperature profiles	No agglomeration		$\eta = 0.25$		$\eta = 0.45$		$\eta = 0.75$	
	FEM	ANN	FEM	ANN	FEM	ANN	FEM	ANN
UTR	1.73	1.70	1.96	1.943	2.07	2.033	2.28	2.227
HT-LB	1.80	1.77	2.05	2.012	2.19	2.142	2.42	2.395
LT-HB	1.65	1.64	1.82	1.794	1.92	1.898	2.06	2.004

Table 9. Effect of complete agglomeration state ($\eta = 1.0$) and different temperature profiles on the central deflection of plate as predicted by in-house developed FEM and ANN tools ($a/b = 1$; $a/h = 50$; CCCC).

Temperature profiles	No agglomeration		$\mu = 0.75$		$\mu = 0.50$		$\mu = 0.25$	
	FEM	ANN	FEM	ANN	FEM	ANN	FEM	ANN
UTR	1.73	1.70	2.08	2.012	2.39	2.327	2.44	2.387
HT-LB	1.80	1.77	2.17	2.143	2.64	2.438	2.89	2.758
LT-HB	1.65	1.64	1.97	1.954	2.16	2.103	2.23	2.187

$$([S_{16}] + [S_{NL8}])\{s_t\} + [S_{17}]\{s_r\} + [S_{18}]\{s_{r*}\}$$
$$+ [S_{\phi\phi}]\{\phi\} + [S_{\phi\psi}]\{\psi\} = \{F_\phi\} - \{F_{T\phi}\} \quad (28.d)$$

$$([S_{19}] + [S_{NL9}])\{s_t\} + [S_{20}]\{s_r\} + [S_{21}]\{s_{r*}\}$$
$$+ [S_{\psi\phi}]\{\phi\} + [S_{\psi\psi}]\{\psi\} = \{F_\psi\} - \{F_{T\psi}\} \quad (28.e)$$

More generally, Eq. (28) can be expressed as

$$[S_{eq}]\{s_t\} = \{F_{eq}\} \quad (29)$$

$[S_{eq}]$ and $\{F_{eq}\}$ denote equivalent stiffness matrix and force vector, respectively. The detailed procedure to arrive at the Eqs. (28. a–28. e) and the associated stiffness matrices and force vectors are demonstrated in Appendix A and B.

3.5. Artificial neural network

The present research has created the ANN model in MATLAB software. 41,472 data points related to nine inputs (Table 3) collected from the proposed FE formulation were used to train the ANN model. The ANN model was instructed to use 70% of the input data for training

incorporating the Levenberg–Marquardt algorithm. Further, the remaining 30% of data is split into 15% for validation and 15% for testing. In the background, several iterations/trial and error were performed to decide the best scheme for the intended task to extremise the mean square error (MSE) and correction coefficient (R). It was noticed that an ANN model with a single hidden layer with ten neurons was an optimum choice (Figure 2(a)). The minimum mean square error (MSE) was found to be 1.57, and the maximum correction coefficient (R) was obtained as 0.9951. Figure 2(b) depicts the regression results of the trained ANN model with ten neurons. The final architecture of the ANN model with input, hidden and output layers are as shown in Figure 3(a). It can be noticed that a good correlation is achieved. Figure 3(b,c) depicts the performance and error histogram of the ANN model developed.

4. Results and discussion

Primarily, the validation of the proposed FE formulation is carried out. To this end, the deflection of PME plates considered by Sladek et al. [71] is re-solved using the in-house developed computational tool. From Figure 4(a,b), it can be noticed that the results are converging and in good agreement with the literature. Further, extending the verification, Table 4 compares the result of natural frequencies of agglomerated rectangular plates as reported in Ref. [72]. The matching of results ensures that the proposed FE formulation can accurately model the agglomeration of CNTs. The computational efficiency of the proposed FE and trained ANN model is depicted in Figure 5. It can be noticed that both approaches significantly reduce the time as opposed to the commercially available software. This justifies the credibility of the approaches adopted in this study. The clamped (C), simply supported (S), and free (F) constraints can be represented as follows:

$Clamped(C)$:
$$u_o = v_o = w_o = \theta_x = \theta_y = \kappa_x = \kappa_y = \phi = \psi = 0 \quad (30.a)$$

$Simply\ supported(S)$:
$$u_o = \theta_x = \kappa_x \neq 0; v_o = w_o = \phi = \psi = 0\ along\ the\ edge\ x = (0,\ a)$$
$$v_o = \theta_y = \kappa_y \neq 0; u_o = w_o = \phi = \psi = 0\ along\ the\ edge\ y = (0,\ b)$$
$$(30.b)$$

$Free(F)$:
$$u_o = v_o = w_o = \theta_x = \theta_y = \kappa_x = \kappa_y = \phi = \psi \neq 0 \quad (30.c)$$

For further studies, unless and otherwise mentioned, $a/b = 1$; $a/h = 50$; clamped condition (CCCC); $h/h_c = 1.67$; $f_r = 2\%$; $\lambda_o = 0.8$; $V_f = 50\%$

4.1. Effect of core materials

This section studies the influence of different core forms on the deflections of the APC/PME sandwich plate. To this end, the variants of the core, such as a pure polymer (no
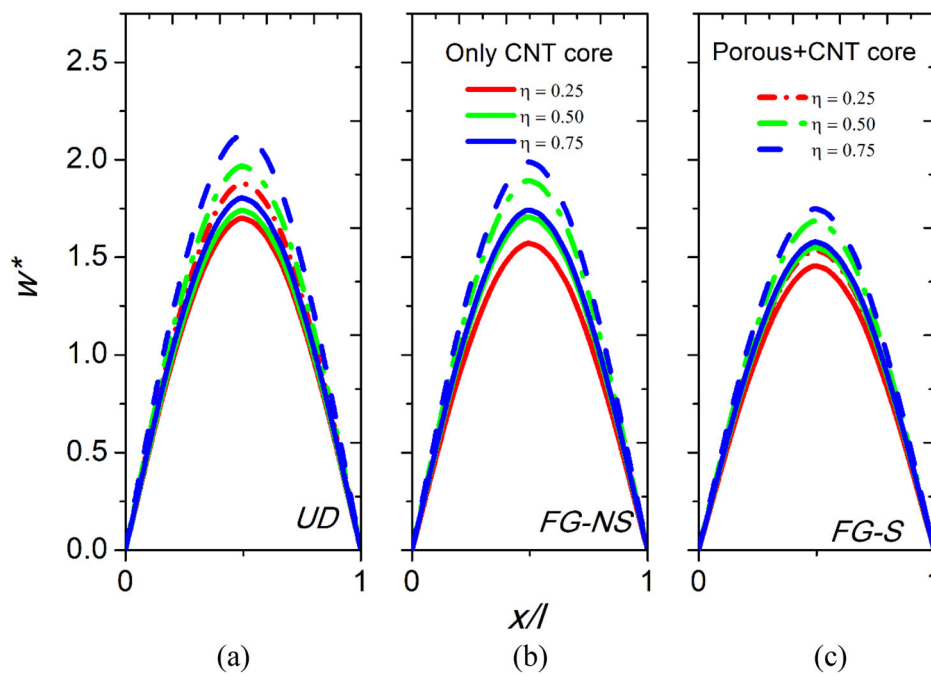
Figure 11. Synergistic influence of the (a) UD (b) FG-NS (c) FG-S porosity patterns and agglomeration on the deflection of APC/PME sandwich plate with partially agglomerated CNT nanocomposite core.
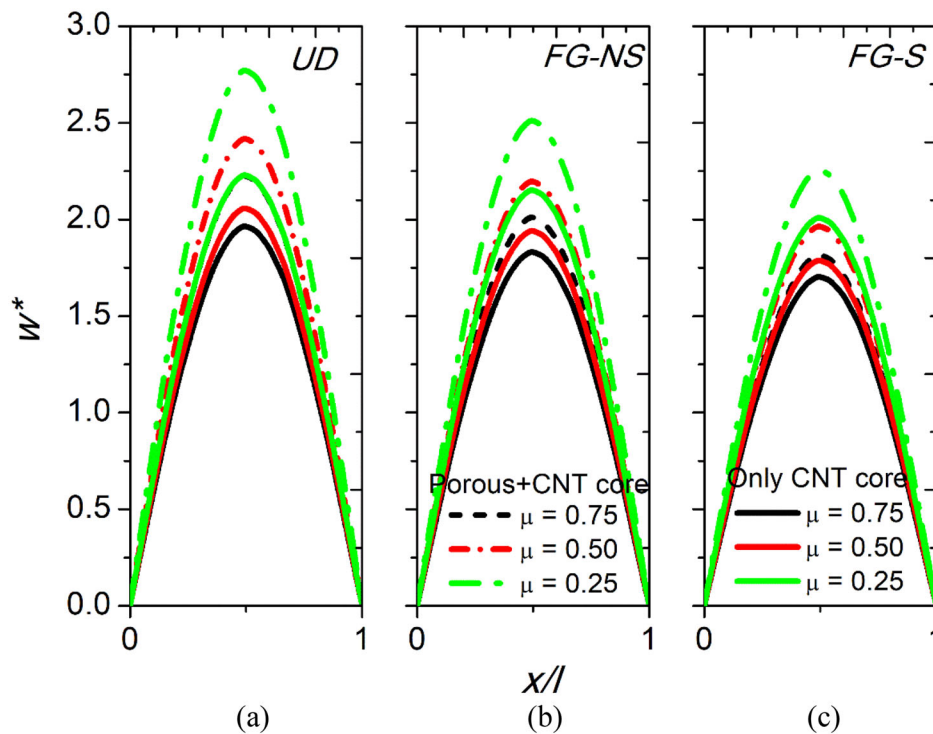

Figure 12. Synergistic influence of the (a) UD (b) FG-NS (c) FG-S porosity patterns and agglomeration on the deflection of APC/PME sandwich plate with completely agglomerated CNT nanocomposite core.

pores, without CNTs), porous (polymer core with pores, no CNTs), and CNT reinforced nanocomposite core (CNT-NCC) (polymer core with CNTs and no pores) are considered. A uniform temperature gradient is assumed for this evaluation. It can be inferred from Figure 6 that among all the core variants selected for assessment, reduced deflections are noticed for CNT-NCC, followed by the pure polymer and porous polymer cores. This might be attributed to the

greater stiffness that CNTs will impart to the polymer core. On the other hand, embedding pores in the polymer core reduces the structure's stiffness and is prone to severe deflection. A detailed assessment of Figure 6 also suggests that the pyro-coupling effect is more for the APC/PME sandwich plate with a porous polymer core. The additional loading effect caused by the pyro-electric and pyro-magnetic field interaction of the PME facesheets magnifies the

Table 10. Effect of porosity patterns ($\lambda_o = 0.2$) and different temperature profiles on the central deflection of plate with partial agglomeration ($\mu = 0.50$) as predicted by in-house developed FEM and ANN tools ($a/b = 1$; $a/h = 50$; CCCC).

Porosity patterns	$\eta = 0.25$		$\eta = 0.45$		$\eta = 0.75$	
	Uniform temperature profile					
	FEM	ANN	FEM	ANN	FEM	ANN
UD	2.43	2.406	2.68	2.591	2.94	2.897
FG-NS	2.11	2.098	2.48	2.387	2.62	2.598
FG-S	1.99	1.967	2.27	2.213	2.39	2.287
	HT-LB temperature profile					
UD	2.56	2.517	2.89	2.831	3.13	3.084
FG-NS	2.21	2.178	2.51	2.485	2.76	2.721
FG-S	2.87	2.756	3.06	3.016	3.42	3.395
	LT-HB temperature profile					
UD	2.04	1.989	2.32	2.284	2.57	2.532
FG-NS	1.86	1.796	2.02	1.988	2.16	2.126
FG-S	1.92	1.873	2.14	2.099	2.31	2.269

Table 11. Effect of porosity patterns and different temperature profiles on the central deflection of plate with complete agglomeration ($\eta = 1.0$) as predicted by in-house developed FEM and ANN tools ($a/b = 1$; $a/h = 50$; CCCC).

Porosity patterns	$\mu = 0.75$		$\mu = 0.50$		$\mu = 0.25$	
	FEM	ANN	FEM	ANN	FEM	ANN
UD	2.46	2.431	2.84	2.823	3.06	3.012
FG-NS	2.23	2.226	2.61	2.596	2.87	2.822
FG-S	2.19	2.175	2.48	2.473	2.57	2.481
	HT-LB temperature profile					
UD	2.96	2.878	3.13	3.081	3.62	3.566
FG-NS	2.65	2.585	2.88	2.832	3.06	3.019
FG-S	3.07	3.00	3.36	3.297	3.95	3.874
	LT-HB temperature profile					
UD	2.38	2.335	2.65	2.596	2.87	2.793
FG-NS	2.00	1.957	2.24	2.190	2.33	2.260
FG-S	2.13	2.078	2.39	2.321	2.48	2.416

Figure 13. The geometry of skew APC/PME sandwich plate with transformed coordinate axes.

influence on the deflection amplitude is noted for the linear temperature (HT-LB) profile. Analogously, Table 6 depicts the central deflection predicted by the ANN model for the sandwich plate. For all the temperature profiles and porosity patterns, the results match very well with the FE results.

4.3. Effect of porosity volume

In Figure 8(a,b), the effect of porosity volume associated with the pyro-coupling on the nonlinear deflections of the APC/PME sandwich plate is investigated and plotted. Table 7 shows the ANN predicted values for the same parametric study. For brevity, only the UD type of porosity distribution is considered for evaluation. As expected, the higher porosity volume results in greater deflection amplitude and pyro-coupling effects. This is because, with the higher porosity volume, the structures' cross section becomes weaker and loses its stiffness. These effects are more predominant for the LTR temperature than the UTR profile due to the higher coupling between the thermal and elastic fields. Further, the discrepancies between the vibration amplitude of APC/PME sandwich plate considering and neglecting the pyro-coupling increase with higher porosity volume, while it diminishes for $\lambda_o = 0.2$, i.e., 20% porosity volume.

4.4. Effect of agglomeration state

Figures 9 and 10 depict the nonlinear deflection of the APC/PME sandwich plate with agglomerated CNT-NCC. The ANN prediction of the same is shown in Tables 8 and 9 for the partial and complete agglomeration states. The effect of parameters η and μ are also considered to realize partial and complete agglomeration states. It is affirmed through this study that higher and lower values of μ and η are beneficial for reduced deflections of APC/PME sandwich

deflection amplitude. Due to coupling effects, pyro-loads' influence is severe for porous core in contrast to the other two. Further, Table 5 extends the same analysis for other temperature profiles and compares the central deflection values obtained from the proposed FE and ANN model. The results predicted by the ANN model agree with the FE results.

4.2. Effect of porosity pattern and temperature profile

Considering the APC/PME sandwich plate with a porous polymer core, the effect of porosity patterns associated with the pyro-coupling on its deflection is investigated. In addition, the influence of different temperature profiles is also studied. From Figure 7(a–c), it is evident that the influence of porosity on the deflection does not follow a generalized trend but depends on the temperature profile. The trend of $UD > FG\text{-}NS > FG\text{-}S$, $UD > FG\text{-}S > FG\text{-}NS$ and $FG\text{-}S > UD > FG\text{-}NS$ is followed for uniform temperature, linear temperature (LT-HB) and linear temperature (HT-LB) profiles, respectively. In addition, the pyro-coupling effect also follows the same trend. This can be attributed to the variation in the temperature profile across the thickness of the APC/PME sandwich plate. Meanwhile, among the different temperature profiles considered for assessment, a significant
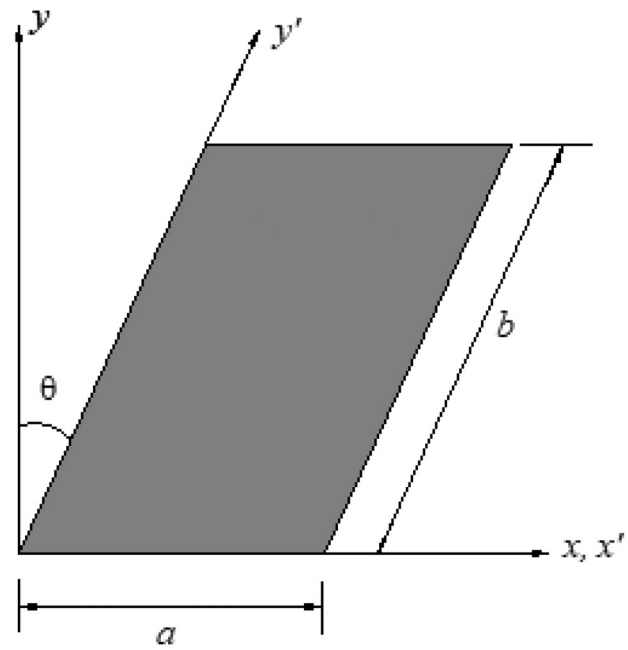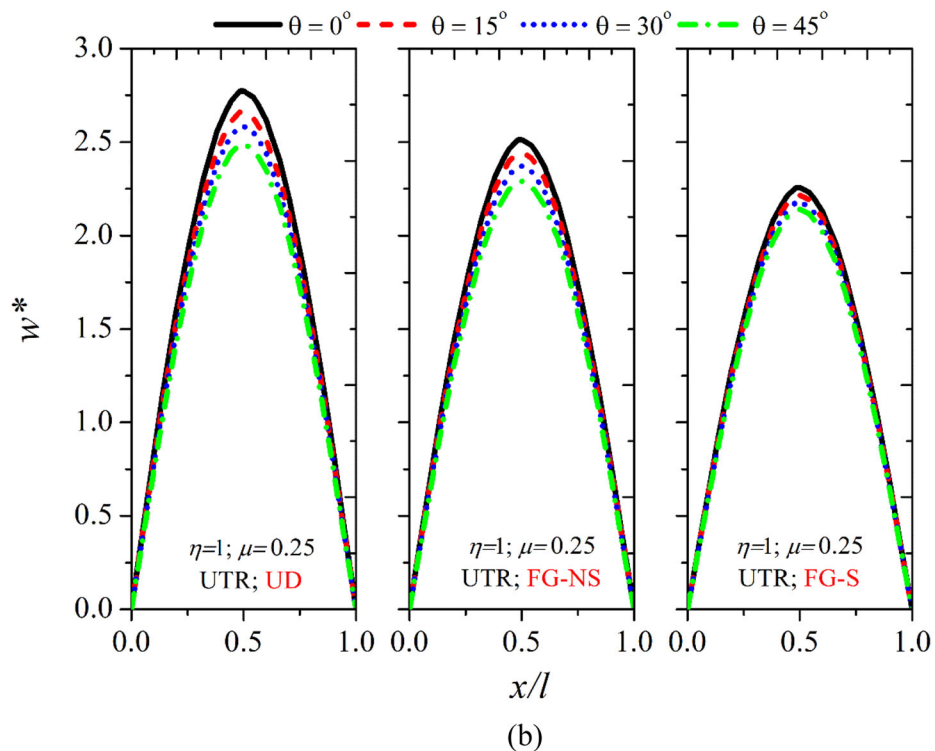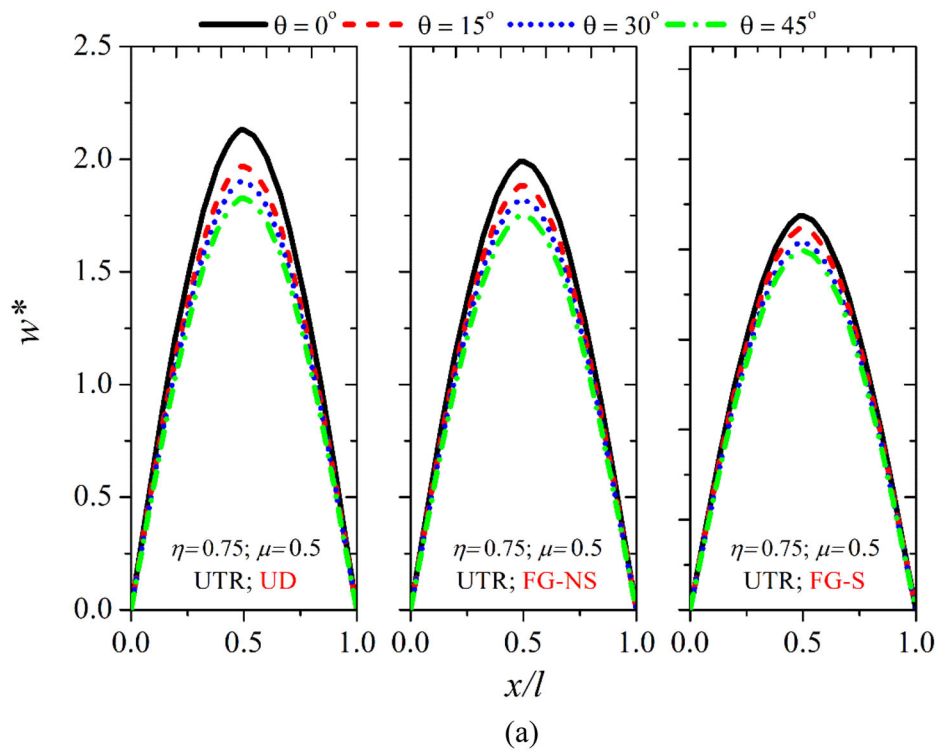
(a)

(b)

Figure 14. Influence of the skew angle on the deflection of APC/PME sandwich plate with (a) partial (b) complete agglomerated CNT nanocomposite core with different porosity distribution ($a/b = 1$; $a/h = 50$; CCCC; $f_r = 2\%$; $\lambda_o = 0.8$; $V_f = 50\%$).

plate with CNT-NCC. Further, the effect of agglomeration associated with pyro-coupling appears to be significant when SSP is subjected to the LTR profile.

Meanwhile, the complete agglomeration state generates a higher amplitude than the partial state. The reason is obvious that partial agglomeration yields better stiffness than complete agglomeration. Also, the associated pyro-coupling

effect is predominant for APC/PME sandwich plates with completely agglomerated NCC.

4.5. Combined effects of porosity and agglomeration

The study is extended to investigate the integrated effects of porosity and agglomeration on the nonlinear deflection of SSP

Table 12. Effect of skew angle and different temperature profiles on the central deflection of plate with partial agglomeration ($\mu = 0.50$) as predicted by in-house developed FEM tool ($a/b = 1$; $a/h = 50$; CCCC).

Porosity patterns	$\theta = 15^o$	$\theta = 30^o$	$\theta = 45^o$
Uniform temperature profile			
UD	1.97	1.90	1.83
FG-NS	1.88	1.82	1.75
FG-S	1.69	1.63	1.59
HT-LB temperature profile			
UD	2.16	2.28	2.64
FG-NS	1.93	2.10	2.23
FG-S	2.24	2.45	2.88
LT-HB temperature profile			
UD	1.55	1.43	1.29
FG-NS	1.26	1.21	1.08
FG-S	1.34	1.29	1.15

Table 13. Effect of skew angle and different temperature profiles on the central deflection of plate with complete agglomeration ($\mu = 0.50$) as predicted by in-house developed FEM tool ($a/b = 1$; $a/h = 50$; CCCC).

Porosity patterns	$\theta = 15^o$	$\theta = 30^o$	$\theta = 45^o$
Uniform temperature profile			
UD	2.66	2.58	2.49
FG-NS	2.44	2.37	2.29
FG-S	2.21	2.18	2.14
HT-LB temperature profile			
UD	2.95	3.12	3.61
FG-NS	2.64	2.87	3.05
FG-S	3.06	3.35	3.94
LT-HB temperature profile			
UD	2.14	1.97	1.78
FG-NS	1.74	1.67	1.49
FG-S	1.85	1.78	1.58

subjected to UTR. To this end, different combinations of η and μ and porosity distributions and volume fractions are considered. Firstly, considering the partial agglomerated state, the effect of introducing different porosity patterns in the already agglomerated CNT-NCC is studied. Hence, in Figure 11(a–c), the variation of central deflection amplitude is plotted for the different values of η. It can be witnessed from these figures that the discrepancies in the peak amplitude of the deflection curves are minimum for the FG-S type of porosity and lower values of η. In other words, introducing porosity in the APC/PME sandwich plate with agglomerated CNT-NCC minimizes its stiffness. Meanwhile, a pronounced effect is seen for UD distribution.

Similarly, the numerical evaluation is extended for the complete agglomeration state by varying the values of μ and displayed in Figure 12(a–c). Unlike the previous observation, a greater influence of porosity is seen for lower values of μ. As discussed in the previous section, a similar variation trend also holds good for the porosity distribution patterns. The pyro-coupling effect of the APC/PME sandwich plate with agglomerated CNT-NNC but without pores is lesser than that of the same plate configuration, including pores. Tables 10 and 11 extend the analysis for other temperature profiles using the ANN technique.

4.6. Effect of skew angle

The influential role of the proposed FE model becomes relevant when analyzing structures other than the conventional
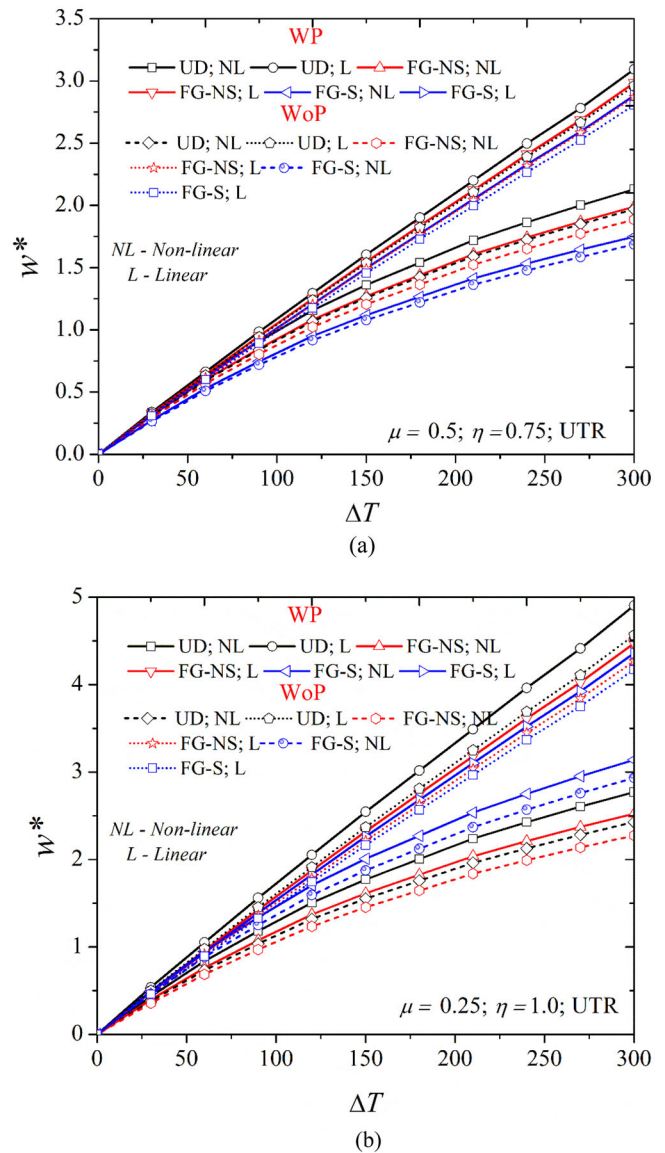

Figure 15. Influence of nonlinearity associated with the deflection of APC/PME sandwich plate with (a) partial (b) complete agglomerated CNT nanocomposite core with different porosity distribution ($a/b = 1$; $a/h = 50$; CCCC; UTR; $f_r = 2\%$; $\lambda_o = 0.8$; $V_f = 50\%$).

rectangular plate. To this end, the evaluation is further extended to investigate the influence of geometrical skewness on the nonlinear central deflections of the APC/PME sandwich plate. As shown in Figure 13, the irregularity in the rectangular coordinates (x, y) is created by tilting them by a skew angle 'θ'. The skewed coordinate axes are denoted by x' and y'. For better understanding, the skewness is represented only with y' axis (Figure 13). Along the skew edges, the stiffness and coupling properties vary significantly. Unlike conventional analytical methods, these variations are well captured by the proposed FE method. It can be seen from Figure 14(a,b) that for both partial and complete agglomerated states, a higher skew angle (θ) results in reduced central deflection. This may be attributed to the fact that the area of the plate diminishes, which in turn, enhances the plate's stiffness.

Further, as opposed to a complete agglomeration state, a slightly higher influence of skewness is noticed for partial agglomeration. In addition, APC/PME sandwich plate with FG-
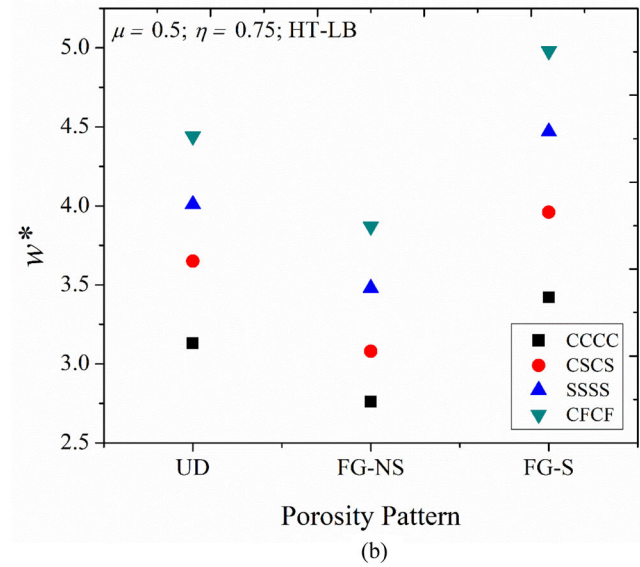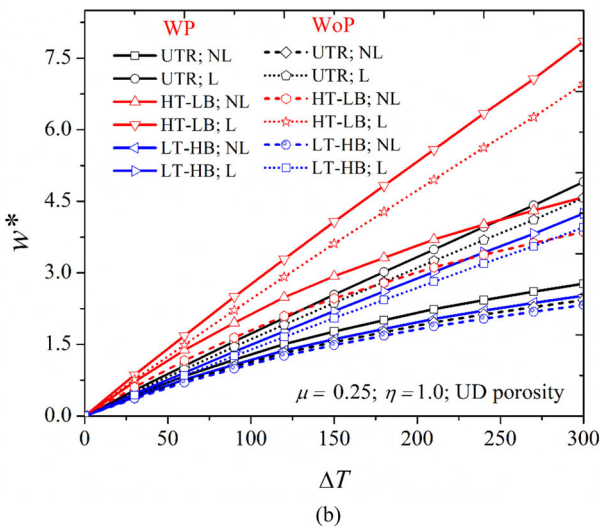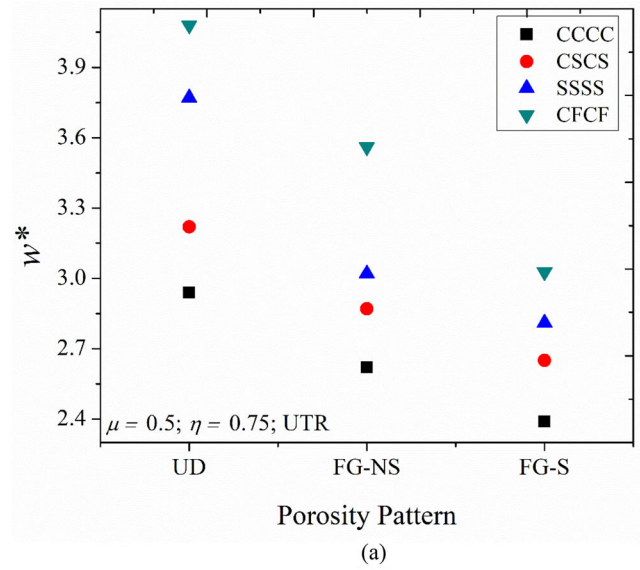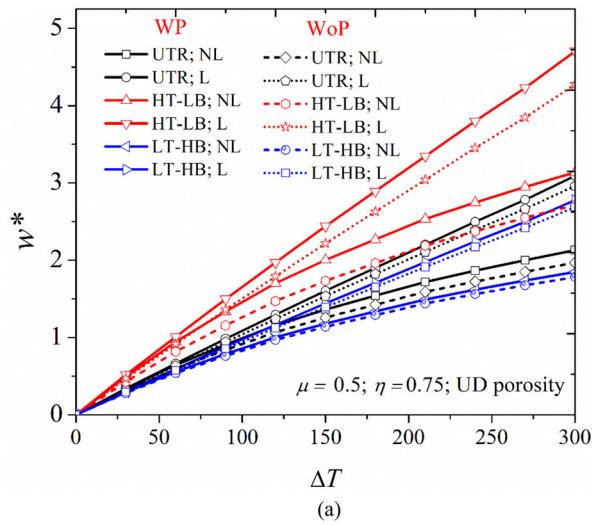
Figure 16. Influence of nonlinearity associated with the deflection of APC/PME sandwich plate with (a) partial (b) complete agglomerated CNT nanocomposite core subjected to different loading conditions ($a/b = 1$; $a/h = 50$; CCCC; UD; $f_r = 2\%$; $\lambda_o = 0.8$; $V_f = 50\%$).
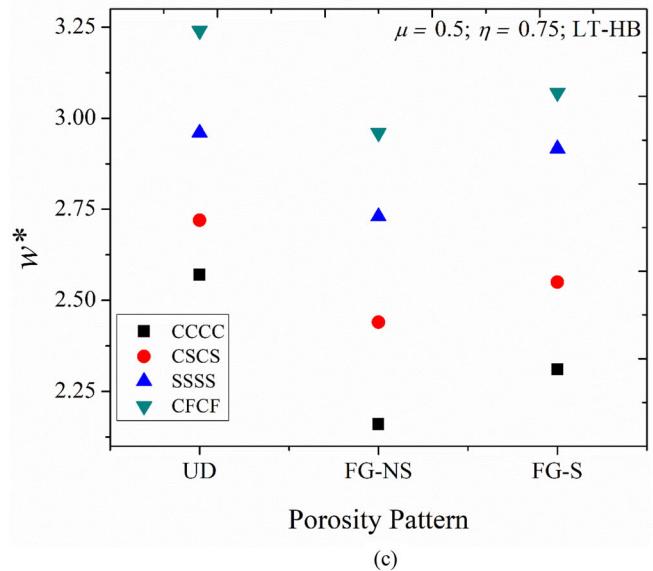

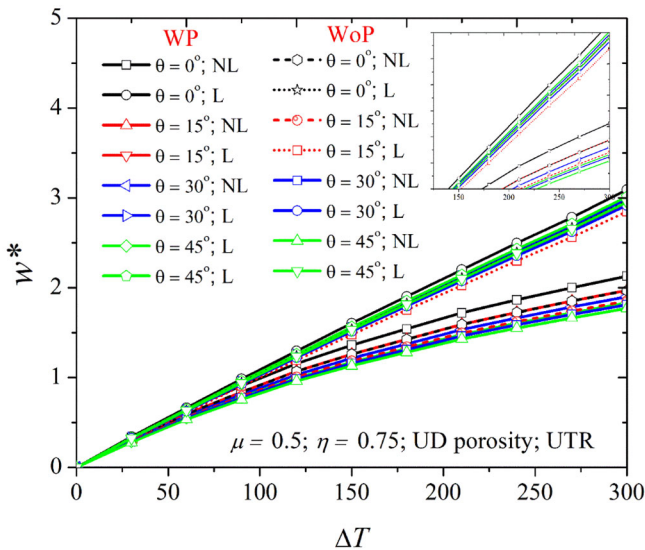**Figure 17.** Influence of nonlinearity associated with the deflection of APC/PME sandwich plate with different skew angles ($a/b = 1$; $a/h = 50$; CCCC; $f_r = 2\%$; $\lambda_o = 0.8$; $V_f = 50\%$).

Figure 18. Influence of boundary conditions associated with the deflection of APC/PME sandwich plate with partially agglomerated CNT nanocomposite core subjected to (a) UTR (b) HT-LB (c) LT-HB temperature conditions.

S porosity displays the negligible effect of skewness. The study is extended for different temperature profiles in Tables 12 and 13 for partial and complete agglomeration states, respectively.

4.7. Effect of nonlinearity

The large deformations in nonlinear regimes behave uniquely and can severely affect the structural integrity. Therefore, this section attempts to compare the linear and nonlinear deflection response of APC/PME sandwich plates subjected to various thermal loads. At first, the integrated effects of porosity and agglomeration on the APC/PME sandwich plate's deflection responses are assessed. From Figures 15 and 16, it can be that realized that the APC/PME sandwich plate exhibits a stiffening type of nonlinearity. The central deflection in the nonlinear regime is lesser than that observed in the linear regime. Further, the degree of pyro-coupling is higher when the plate is operated in the nonlinear regime. This may be due to the enhanced coupling resulting from the nonlinear displacement component. The influence of nonlinearity is predominant for the completely agglomerated state and HT-LB temperature profiles due to the enhanced strains developed. Figure 17 shows the effect of skewness associated with the pyro-coupling on the linear and nonlinear deflections. It can be seen that pyro-coupling is predominant for a rectangular APC/PME sandwich plate ($\theta = 0^o$).

4.8. Effect of boundary conditions

This section presents a brief insight into the effect of boundary conditions on the nonlinear deflections of the APC/PME sandwich plate. To this end, only the partially agglomerated state is considered. It can be seen from Figure 18(a–c) that the central deflections are minimum for fully clamped constraint. This is followed by CSCS, SSSS and CFCF conditions. The effect of boundary conditions is predominant for those porosity patterns which exhibit higher deflection of APC/PME sandwich plate corresponding to different temperature profiles, as discussed in Section 4.2.

5. Conclusions

This research article investigates the nonlinear deflections of smart sandwich plates exposed to various thermal fields through an in-house developed finite element (FE) and artificial neural network (ANN) based data-driven prediction tools. The 41472 simulation data points obtained from the FE analysis were used to train, test, and validate the ANN model. The ANN model with a single hidden layer and ten neurons was instructed to use 70% of the input data for training incorporating the Levenberg–Marquardt algorithm. The nanocomposite core of the plate is assumed to be made of agglomerated CNTs and pores. The facings are of piezo-magneto-elastic (PME) material with a different volume fraction of piezoelectric and piezomagnetic phases. The synergistic influence of pyro-coupling, agglomeration, and porosity on the nonlinear central deflections of the smart plate is investigated in detail. The numerical results reveal that

HT-LB exhibits a predominant effect among the selected temperature profiles. Meanwhile, the FG-S type of porosity significantly reduces the stiffness of the smart sandwich plate. The degree of pyro-coupling is significantly influenced by the temperature profiles and porosity parameters (volume and distributions). The deflection of the plate with a partially agglomerated CNT core is lesser than the completely agglomerated core. However, the pyro-coupling effects are more for the case of complete agglomeration. The proposed FE model displays an upper hand over the conventional analytical models through its flexibility to simulate nonlinear deflections of skewed plates. The comparison studies show that by using the ANN approach, the computational efforts can be significantly reduced without compromising accuracy. Therefore, the FEE-ANN model can be further used for different coupled structural analyses of PME composites.

Data availability

The raw/processed data required to reproduce these findings cannot be shared at this time as the data also forms part of an ongoing study.

References

[1] T.Q. Quan, V.M. Anh, V. Mahesh, and N.D. Duc, Vibration and nonlinear dynamic response of imperfect sandwich piezo-electric auxetic plate, Mech. Adv. Mater. Struct., vol. 29, no. 1, pp. 127–137, 2022. DOI: 10.1080/15376494.2020.1752864.

[2] A.F. Mota, M.A.R. Loja, J. Infante Barbosa, and M. Vinyas, Mechanical behavior of a sandwich plate with aluminum foam core, using an image-based layerwise model, Mech. Adv. Mater. Struct., vol. 29, no. 25, pp. 4074–4095, 2022. DOI: 10.1080/15376494.2021.1919801.

[3] A. Gorgeri, R. Vescovini, and L. Dozio, Sublaminate variable kinematics shell models for functionally graded sandwich panels: Bending and free vibration response, Mech. Adv. Mater. Struct., vol. 29, no. 1, pp. 15–32, 2022. DOI: 10.1080/15376494.2020.1749738.

[4] K. Koutoati, F. Mohri, and E.M. Daya, Finite element approach of axial bending coupling on static and vibration behaviors of functionally graded material sandwich beams, Mech. Adv. Mater. Struct., vol. 28, no. 15, pp. 1537–1553, 2021. DOI: 10.1080/15376494.2019.1685144.

[5] M. Hachemi, Vibration analysis of variable stiffness laminated composite sandwich plates, Mech. Adv. Mater. Struct., vol. 27, no. 19, pp. 1687–1700, 2020. DOI: 10.1080/15376494.2018.1524951.

[6] S.M.R. Khalili, M.M. Kheirikhah, and K. Malekzadeh Fard, Buckling analysis of composite sandwich plates with flexible core using improved high-order theory, Mech. Adv. Mater. Struct., vol. 22, no. 4, pp. 233–247, 2015. DOI: 10.1080/15376494.2012.736051.

[7] Z. Wu, J. Wu, F. Lu, C. Zhang, Z. Liu, and Y. Zhu, Free vibration analysis and multi-objective optimization of lattice sandwich beams, Mech. Adv. Mater. Struct., pp. 1–14, 2023. DOI: 10.1080/15376494.2023.2189333.

[8] A. Eyvazian, T.A. Sebaey, K.K. Żur, A. Khan, H. Zhang, and S.H. Wong, On the dynamics of FG-GPLRC sandwich cylinders based on an unconstrained higher-order theory, Compos.

Struct., vol. 267, pp. 113879, 2021. DOI: 10.1016/j.compstruct.2021.113879.

[9] A.R. Setoodeh, M. Shojaee, and P. Malekzadeh, Vibrational behavior of doubly curved smart sandwich shells with FG-CNTRC face sheets and FG porous core, Comp. B: Eng., vol. 165, pp. 798–822, 2019. DOI: 10.1016/j.compositesb.2019.01.022.

[10] R. Moradi-Dastjerdi and K. Behdinan, Stability analysis of multifunctional smart sandwich plates with graphene nanocomposite and porous layers, Int. J. Mech. Sci., vol. 167, pp. 105283, 2020. DOI: 10.1016/j.ijmecsci.2019.105283.

[11] R. Moradi-Dastjerdi and F. Aghadavoudi, Static analysis of functionally graded nanocomposite sandwich plates reinforced by defected CNT, Compos. Struct., vol. 200, pp. 839–848, 2018. DOI: 10.1016/j.compstruct.2018.05.122.

[12] E. Arshid, S. Amir, and A. Loghman, Static and dynamic analyses of FG-GNPs reinforced porous nanocomposite annular micro-plates based on MSGT, Int. J. Mech. Sci., vol. 180, pp. 105656, 2020. DOI: 10.1016/j.ijmecsci.2020.105656.

[13] E. Arshid, S. Amir, and A. Loghman, Thermal buckling analysis of FG graphene nanoplatelets reinforced porous nanocomposite MCST-based annular/circular microplates, Aerosp. Sci. Technol., vol. 111, pp. 106561, 2021. DOI: 10.1016/j.ast.2021.106561.

[14] E. Arshid, S. Amir, and A. Loghman, Bending and buckling behaviors of heterogeneous temperature-dependent micro annular/circular porous sandwich plates integrated by FGPEM nano-Composite layers, J. Sandw. Struct. Mater., vol. 23, no. 8, pp. 3836–3877, 2021. DOI: 10.1177/1099636220955027.

[15] Ehsan Arshid and Saeed Amir, Size-dependent vibration analysis of fluid-infiltrated porous curved microbeams integrated with reinforced functionally graded graphene platelets face sheets considering thickness stretching effect, Proc. Inst. Mech. Eng., L: J. Mater.: Des. Appl., vol. 235, no. 5, pp. 1077–1099, 2021. DOI: 10.1177/1464420720985556.

[16] E. Arshid, M. Khorasani, Z. Soleimani-Javid, S. Amir, and A. Tounsi, Porosity-dependent vibration analysis of FG microplates embedded by polymeric nanocomposite patches considering hygrothermal effect via an innovative plate theory, Eng. Comput., vol. 38, no. S5, pp. 4051–4072, 2022. DOI: 10.1007/s00366-021-01382-y.

[17] Z.X. Wang, H.S. Shen, and L. Shen, Thermal postbuckling analysis of sandwich beams with functionally graded auxetic GRMMC core on elastic foundations, J. Therm. Stresses., vol. 44, no. 12, pp. 1479–1494, 2021. DOI: 10.1080/01495739.2021.1994902.

[18] X.K. Xia and H.S. Shen, Vibration of post-buckled sandwich plates with FGM face sheets in a thermal environment, J. Sound Vib., vol. 314, no. 1–2, pp. 254–274, 2008. DOI: 10.1016/j.jsv.2008.01.019.

[19] M. Mirzaei and Y. Kiani, Snap-through phenomenon in a thermally postbuckled temperature dependent sandwich beam with FG-CNTRC face sheets, Compos. Struct., vol. 134, pp. 1004–1013, 2015. DOI: 10.1016/j.compstruct.2015.09.003.

[20] R.P. Khandelwal, A. Chakrabarti, and P. Bhargava, Efficient 2D thermo-mechanical analysis of composites and sandwich laminates, Mech. Adv. Mater. Struct., vol. 26, no. 6, pp. 526–538, 2019. DOI: 10.1080/15376494.2017.1410897.

[21] C.S. Chen, F.H. Liu, and W.R. Chen, Dynamic characteristics of functionally graded material sandwich plates in thermal environments, Mech. Adv. Mater. Struct., vol. 24, no. 2, pp. 157–167, 2017. DOI: 10.1080/15376494.2015.1124949.

[22] A.M. Zenkour and N.A. Alghamdi, Bending analysis of functionally graded sandwich plates under the effect of mechanical and thermal loads, Mech. Adv. Mater. Struct., vol. 17, no. 6, pp. 419–432, 2010. DOI: 10.1080/15376494.2010.483323.

[23] S. Chakraborty, T. Dey, V. Mahesh, and D. Harursampath, Post-buckling and vibration analysis of randomly distributed CNT reinforced fibre composite plates under localised heating, Mech. Adv. Mater. Struct., pp. 1–20, 2022. DOI: 10.1080/15376494.2022.2095470.

[24] A. Karakoti, S. Pandey, and V.R. Kar, Nonlinear transient analysis of porous P-FGM and S-FGM sandwich plates and shell panels under blast loading and thermal environment, Thin-Walled Struct., vol. 173, pp. 108985, 2022. DOI: 10.1016/j.tws.2022.108985.

[25] K. Khorshidi and M. Karimi, Flutter analysis of sandwich plates with functionally graded face sheets in thermal environment, Aerosp. Sci. Technol., vol. 95, pp. 105461, 2019. DOI: 10.1016/j.ast.2019.105461.

[26] H.S. Shen and C.L. Zhang, Thermal buckling and postbuckling behavior of functionally graded carbon nanotube-reinforced composite plates, Mater. Des., vol. 31, no. 7, pp. 3403–3411, 2010. DOI: 10.1016/j.matdes.2010.01.048.

[27] H.S. Shen, Postbuckling of nanotube-reinforced composite cylindrical shells in thermal environments, Part I: Axially-loaded shells, Compos. Struct., vol. 93, no. 8, pp. 2096–2108, 2011. DOI: 10.1016/j.compstruct.2011.02.011.

[28] H.S. Shen, Y. Xiang, and J.N. Reddy, Thermal postbuckling behavior of FG-GRC laminated cylindrical panels with temperature-dependent properties, Compos. Struct., vol. 211, pp. 433–442, 2019. DOI: 10.1016/j.compstruct.2018.12.023.

[29] J. Yang, X.H. Huang, and H.S. Shen, Nonlinear vibration of temperature-dependent FG-CNTRC laminated plates with negative Poisson's ratio, Thin-Walled Struct., vol. 148, pp. 106514, 2020. DOI: 10.1016/j.tws.2019.106514.

[30] M. Vinyas, Computational analysis of smart magneto-electro-elastic materials and structures: Review and classification, Arch. Computat. Methods Eng., vol. 28, no. 3, pp. 1205–1248, 2021. DOI: 10.1007/s11831-020-09406-4.

[31] V. Mahesh, Nonlinear damping of auxetic sandwich plates with functionally graded magneto-electro-elastic facings under multiphysics loads and electromagnetic circuits, Compos. Struct., vol. 290, pp. 115523, 2022. DOI: 10.1016/j.compstruct.2022.115523.

[32] V. Mahesh, Active control of nonlinear coupled transient vibrations of multifunctional sandwich plates with agglomerated FG-CNTs core/magneto-electro-elastic facesheets, Thin-Walled Struct., vol. 179, pp. 109547, 2022. DOI: 10.1016/j.tws.2022.109547.

[33] M. Vinyas, Vibration control of skew magneto-electro-elastic plates using active constrained layer damping, Compos. Struct., vol. 208, pp. 600–617, 2019. DOI: 10.1016/j.compstruct.2018.10.046.

[34] V. Mahesh and A.S. Mangalasseri, Agglomeration effects of CNTs on the energy harvesting performance of multifield interactive magneto-electro-elastic/nanocomposite unimorph smart beam, Mech. Based Des. Struct. Mach., pp. 1–27, 2022. DOI: 10.1080/15397734.2022.2144886.

[35] Kanav Chadha, Vinyas Mahesh, Arjun Siddharth Mangalasseri, and Vishwas Mahesh, On analysing vibration energy harvester with auxetic core and magneto-electro-elastic facings, Thin-Walled Struct., vol. 184, pp. 110533, 2023. DOI: 10.1016/j.tws.2023.110533.

[36] A. Siddharth Mangalasseri, V. Mahesh, V. Mahesh, S.A. Ponnusami, and D. Harursampath, Investigation on the interphase effects on the energy harvesting characteristics of three phase magneto-electro-elastic cantilever beam, Mech. Adv. Mater. Struct., pp. 1–13, 2022. DOI: 10.1080/15376494.2022.2062630.

[37] V. Mahesh, A numerical investigation on the nonlinear pyro-coupled dynamic response of blast loaded magnetoelectroelastic multiphase porous plates in thermal environment, Eur. Phys. J. Plus., vol. 137, no. 5, pp. 1–24, 2022. DOI: 10.1140/epjp/s13360-022-02795-4.

[38] V. Mahesh, Nonlinear pyrocoupled dynamic response of functionally graded magnetoelectroelastic plates under blast loading in thermal environment, Mech. Based Des. Struct. Mach., pp. 1–26, 2022. DOI: 10.1080/15397734.2022.2047723.

[39] F. Ramirez, P.R. Heyliger, and E. Pan, Discrete layer solution to free vibrations of functionally graded magneto-electro-elastic plates, Mech. Adv. Mater. Struct., vol. 13, no. 3, pp. 249–266, 2006. DOI: 10.1080/15376490600582750.

[40] J. Sladek, V. Sladek, S. Krahulec, C.S. Chen, and D.L. Young, Analyses of circular magnetoelectroelastic plates with functionally graded material properties, Mech. Adv. Mater. Struct., vol. 22, no. 6, pp. 479–489, 2015. DOI: 10.1080/15376494.2013.807448.

[41] G. Davì, A. Milazzo, and C. Orlando, Magneto-electro-elastic bimorph analysis by the boundary element method, Mech. Adv. Mater. Struct., vol. 15, no. 3–4, pp. 220–227, 2008. DOI: 10.1080/15376490801907715.

[42] V. Mahesh, Nonlinear free vibration of multifunctional sandwich plates with auxetic core and magneto-electro-elastic facesheets of different micro-topological textures: FE approach, Mech. Adv. Mater. Struct., vol. 29, no. 27, pp. 6266–6287, 2022. DOI: 10.1080/15376494.2021.1974619.

[43] V.D. Quang, T.Q. Quan, and P. Tran, Static buckling analysis and geometrical optimisation of magneto-electro-elastic sandwich plate with auxetic honeycomb core, Thin-Walled Struct., vol. 173, pp. 108935, 2022. DOI: 10.1016/j.tws.2022.108935.

[44] N.D. Dat, T.Q. Quan, and N.D. Duc, Vibration analysis of auxetic laminated plate with magneto-electro-elastic face sheets subjected to blast loading, Compos. Struct., vol. 280, pp. 114925, 2022.

[45] B. Nie, G. Meng, S. Ren, J. Wang, Z. Ren, L. Zhou, and P. Liu, Stable node-based smoothed radial point interpolation method for the dynamic analysis of the hygro-thermo-magneto-electro-elastic coupling problem, Eng. Anal. Boundary Elem., vol. 134, pp. 435–452, 2022. DOI: 10.1016/j.enganabound.2021.10.015.

[46] V. Mahesh and D. Harursampath, Nonlinear deflection analysis of CNT/magneto-electro-elastic smart shells under multi-physics loading, Mech. Adv. Mater. Struct., vol. 29, no. 7, pp. 1047–1071, 2022. DOI: 10.1080/15376494.2020.1805059.

[47] V. Mahesh, Porosity effect on the nonlinear deflection of functionally graded magneto-electro-elastic smart shells under combined loading, Mech. Adv. Mater. Struct., vol. 29, no. 19, pp. 2707–2725, 2022. DOI: 10.1080/15376494.2021.1875086.

[48] Y.F. Zhao, X. Wang, G.Z. Zhao, B. Markert, and S.Q. Zhang, Large deflections of magneto-electro-elastic cylindrical shells reinforced with functionally graded carbon nanotubes, Mech. Adv. Mater. Struct., pp. 1–15, 2023. DOI: 10.1080/15376494.2022.2158507.

[49] F.P. Ewolo Ngak, G.E. Ntamack, and L. Azrar, Coupled state-space and Gauss integration procedures for static analysis of general functionally graded magnetoelectroelastic laminated plates, Mech. Adv. Mater. Struct., vol. 29, no. 11, pp. 1553–1569, 2022. DOI: 10.1080/15376494.2020.1829758.

[50] A. Akbarzadeh and Z. Chen, Thermo-magneto-electro-elastic responses of rotating hollow cylinders, Mech. Adv. Mater. Struct., vol. 21, no. 1, pp. 67–80, 2014. DOI: 10.1080/15376494.2012.677108.

[51] E. Arshid, Z. Soleimani-Javid, S. Amir, and N.D. Duc, Higher-order hygro-magneto-electro-thermomechanical analysis of FG-GNPs-reinforced composite cylindrical shells embedded in PEM layers, Aerosp. Sci. Technol., vol. 126, pp. 107573, 2022. DOI: 10.1016/j.ast.2022.107573.

[52] M. Khorasani, Z. Soleimani-Javid, E. Arshid, S. Amir, and Ö. Civalek, Vibration analysis of graphene nanoplatelets' reinforced composite plates integrated by piezo-electromagnetic patches on the piezo-electromagnetic media, Waves Random Complex Media., pp. 1–31, 2021. DOI: 10.1080/17455030.2021.1956017.

[53] S. Amir, E.M.R. Bidgoli, and E. Arshid, Size-dependent vibration analysis of a three-layered porous rectangular nano plate with piezo-electromagnetic face sheets subjected to pre loads based on SSDT, Mech. Adv. Mater. Struct., vol. 27, no. 8, pp. 605–619, 2020. DOI: 10.1080/15376494.2018.1487612.

[54] S. Amir, E. Arshid, and M.R.G. Arani, Size-dependent magneto-electro-elastic vibration analysis of FG saturated porous annular/circular micro sandwich plates embedded with nano-composite face sheets subjected to multi-physical pre loads. Smart Struct. Syst. Int. J., vol. 23, no. 5, pp. 429–447, 2019.

[55] S. Amir, E. Arshid, Z. Khoddami Maraghi, A. Loghman, and A. Ghorbanpour Arani, Vibration analysis of magnetorheological fluid circular sandwich plates with magnetostrictive facesheets exposed to monotonic magnetic field located on visco-Pasternak substrate, J. Vib. Control., vol. 26, no. 17–18, pp. 1523–1537, 2020. DOI: 10.1177/1077546319899203.

[56] E. Arshid and A.R. Khorshidvand, Free vibration analysis of saturated porous FG circular plates integrated with piezoelectric actuators via differential quadrature method, Thin-Walled Struct., vol. 125, pp. 220–233, 2018. DOI: 10.1016/j.tws.2018.01.007.

[57] Z. Khoddami Maraghi, S. Amir, and E. Arshid, On the natural frequencies of smart circular plates with magnetorheological fluid core embedded between magnetostrictive patches on Kerr elastic substance, Mech. Based Des. Struct. Mach., pp. 1–18, 2022. DOI: 10.1080/15397734.2022.2156885.

[58] M. Vinyas and S.C. Kattimani, Static analysis of stepped functionally graded magneto-electro-elastic plates in thermal environment: A finite element study, Compos. Struct., vol. 178, pp. 63–86, 2017. DOI: 10.1016/j.compstruct.2017.06.068.

[59] M. Vinyas and S.C. Kattimani, Static studies of stepped functionally graded magneto-electro-elastic beam subjected to different thermal loads, Compos. Struct., vol. 163, pp. 216–237, 2017. DOI: 10.1016/j.compstruct.2016.12.040.

[60] V. Mahesh, Nonlinear deflection of carbon nanotube reinforced multiphase magneto-electro-elastic plates in thermal environment considering pyrocoupling effects, Math. Methods in App. Sci., 2020. DOI: 10.1002/mma.6858.

[61] V. Mahesh, Nonlinear pyrocoupled deflection of viscoelastic sandwich shell with CNT reinforced magneto-electro-elastic facing subjected to electromagnetic loads in thermal environment, Eur. Phys. J. Plus., vol. 136, no. 8, pp. 1–30, 2021. DOI: 10.1140/epjp/s13360-021-01751-y.

[62] V. Mahesh, Effect of carbon nanotube-reinforced magneto-electro-elastic facings on the pyrocoupled nonlinear deflection of viscoelastic sandwich skew plates in thermal environment, Proc. Inst. Mech. Eng. L: J. Mater.: Des. Appl., vol. 236, no. 1, pp. 200–221, 2022. DOI: 10.1177/14644207211044093.

[63] S. Haykin, 2009. Neural Networks and Learning Machines, 3/E, Pearson Education India, New Jersey.

[64] Y.S. Al Rjoub and J.A. Alshatnawi, Free vibration of functionally-graded porous cracked plates, Struct., vol. 28, pp. 2392–2403, 2020. DOI: 10.1016/j.istruc.2020.10.059.

[65] D. Atilla, C. Sencan, B. Goren Kiral, and Z. Kiral, Free vibration and buckling analyses of laminated composite plates with cutout, Arch. Appl. Mech., vol. 90, no. 11, pp. 2433–2448, 2020. DOI: 10.1007/s00419-020-01730-2.

[66] V. Kallannavar, S. Kattimani, M.E.M. Soudagar, M.A. Mujtaba, S. Alshahrani, and M. Imran, Neural network-based prediction model to investigate the influence of temperature and moisture on vibration characteristics of skew laminated composite sandwich plates, Mater., vol. 14, no. 12, pp. 3170, 2021. DOI: 10.3390/ma14123170.

[67] D.L. Shi, X.Q. Feng, Y.Y. Huang, K.C. Hwang, and H. Gao, The effect of nanotube waviness and agglomeration on the elastic property of carbon nanotube-reinforced composites, J. Eng. Mater. Technol., vol. 126, no. 3, pp. 250–257, 2004. DOI: 10.1115/1.1751182.

[68] H.S. Shen, Y. Xiang, and F. Lin, Nonlinear bending of functionally graded graphene-reinforced composite laminated plates resting on elastic foundations in thermal environments, Compos. Struct., vol. 170, pp. 80–90, 2017. DOI: 10.1016/j.compstruct.2017.03.001.

[69] M. Mohammadi, M. Bamdad, K. Alambeigi, R. Dimitri, and F. Tornabene, Electro-elastic response of cylindrical sandwich pressure vessels with porous core and piezoelectric face-sheets, Compos. Struct., vol. 225, pp. 111119, 2019. DOI: 10.1016/j.compstruct.2019.111119.

[70] J.N. Reddy, 2003. Mechanics of Laminated Composite Plates and Shells: Theory and Analysis, CRC press, Boca Raton.

[71] J. Sladek, V. Sladek, S. Krahulec, and E. Pan, The MLPG analyses of large deflections of magnetoelectroelastic plates, Eng. Anal. Boundary Elem., vol. 37, no. 4, pp. 673–682, 2013. DOI: 10.1016/j.enganabound.2013.02.001.

[72] D.S. Craveiro and M.A.R. Loja, A study on the effect of carbon nanotubes' distribution and agglomeration in the free vibration of nanocomposite plates, Carbon., vol. 6, no. 4, pp. 79, 2020. DOI: 10.3390/c6040079.

Appendix A

To derive, Eq. (29), the previous equations are condensed based on the d.o.f's as shown:
The Eq. (28. e), is solved in a direct manner to obtain $\{\psi\}$ as follows:

$$\{\psi\} = -[S_{\psi\psi}]^{-1}\left\{ \begin{array}{l} ([S_{19}] + [S_{NL9}])\{d_t\} + [S_{20}]\{d_r\} + [S_{21}]\{d_{r*}\} \\ +[S_{\phi\psi}]^T\{\phi\} - \{F_\psi\} + \{F_{T\psi}\} \end{array} \right\} \tag{A-1}$$

The term $\{\psi\}$ of Eq. (28. d) is substituted by the Eq. (A-1) and solved for $\{\phi\}$ to get,

$$
\begin{aligned}
&([S_{16}] + [S_{NL8}])\{d_t\} + [S_{17}]\{d_r\} + [S_{18}]\{d_{r*}\} + [S_{\phi\phi}]\{\phi\} \\
&-[S_{\phi\psi}]\left[[S_{\psi\psi}]^{-1}\left(\begin{array}{l} ([S_{19}] + [S_{NL9}])\{s_t\} + [S_{20}]\{s_r\} + [S_{21}]\{s_{r*}\} \\ +[S_{\phi\psi}]^T\{\phi\} - \{F_\psi\} + \{F_{T\psi}\} \end{array} \right) \right] \\
&= \{F_\phi\} - \{F_{T\phi}\} \\
&([S_{22}] + [S_{NL11}])\{s_t\} + [S_{23}]\{s_r\} + [S_{24}]\{s_{r*}\} + [S_{25}]\{\phi\} \\
&+[S_{\phi\phi}][S_{\psi\psi}]^{-1}(\{F_\psi\} - \{F_{T\psi}\}) = (\{F_\phi\} - \{F_{T\phi}\}) \\
&\{\phi\} = \left(\begin{array}{l} -[S_{26}]\{s_t\} - [S_{NL\_12}]\{s_t\} - [S_{27}]\{s_r\} - [S_{28}]\{s_{r*}\} \\ -[S_{F1}](\{F_\psi\} - \{F_{t\psi}\}) - [S_{25}]^{-1}(\{F_\phi\} - \{F_{t\phi}\}) \end{array} \right)
\end{aligned}
\tag{A-2}
$$

Likewise, the terms $\{\psi\}$ and $\{\phi\}$ of Eq. (28. c) is replaced with the Eqs. (A-1) and (A-2) and solved for $\{s_{r*}\}$, to deduce

$$
\begin{aligned}
&([S_{29}] + [S_{NL13}])\{s_t\} + [S_{30}]\{s_r\} + [S_{31}]\{s_{r*}\} + [S_{32}]\{\phi\} \\
&+[S_{F2}](\{F_\psi\} - \{F_{T\psi}\}) = 0 \\
&([S_{33}] + [S_{NL15}])\{s_t\} + [S_{34}]\{s_r\} + [S_{35}]\{s_{r*}\} \\
&+[S_{F5}](\{F_\psi\} - \{F_{T\psi}\}) - [K_{F3}](\{F_\phi\} - \{F_{T\phi}\}) = 0 \\
&\{s_{r*}\} = \left(\begin{array}{l} -[S_{36}]\{s_t\} - [S_{NL\_16}]\{s_t\} - [S_{37}]\{s_r\} \\ -[S_{F6}](\{F_\psi\} - \{F_{T\psi}\}) - [S_{F7}](\{F_\phi\} - \{F_{T\phi}\}) \end{array} \right)
\end{aligned}
\tag{A-3}
$$

In a similar fashion, solving for $\{s_r\}$ by substituting Eqs. (A-1–A-3) in Eq. (28. b), we obtain,

$$
\begin{aligned}
&([S_{38}] + [S_{NL18}])\{s_t\} + [S_{39}]\{s_r\} + [S_{40}]\{s_{r*}\} + [S_{41}]\{\phi\} \\
&+[S_{F8}](\{F_\psi\} - \{F_{T\psi}\}) = 0 \\
&([S_{42}] + [S_{NL20}])\{s_t\} + [S_{43}]\{s_r\} + [S_{44}]\{s_{r*}\} \\
&+[S_{F11}](\{F_\psi\} - \{F_{T\psi}\}) - [S_{F10}](\{F_\phi\} - \{F_{T\phi}\}) = 0 \\
&([S_{45}] + [S_{NL22}])\{s_t\} + [S_{46}]\{s_r\} \\
&+[S_{F15}](\{F_\psi\} - \{F_{T\psi}\}) - [S_{F14}](\{F_\phi\} - \{F_{T\phi}\}) = 0 \\
&\{s_r\} = \left(\begin{array}{l} -[S_{47}]\{s_t\} - [S_{NL\_23}]\{s_t\} \\ -[S_{F17}](\{F_\psi\} - \{F_{t\psi}\}) + [S_{F16}](\{F_\phi\} - \{F_{t\phi}\}) \end{array} \right)
\end{aligned}
\tag{A-4}
$$

Finally, using Eqs. (A-1–A-4) in Eq. (28. a), $\{s_t\}$ is derived along with the equivalent matrices $[S_{eq}]$ and $[S_{NL\_eq}]$ as follows:

$$
\begin{aligned}
&([S_{48}] + [S_{NL\_24}])\{d_t\} + ([S_{49}] + [S_{NL\_25}])\{d_r\} + ([S_{50}] + [S_{NL\_26}])\{d_{r*}\} \\
&+([S_{51}] + [S_{NL\_27}])\{\phi\} + [S_{F20}](\{F_\psi\} - \{F_{t\psi}\}) = \{F_t\} \\
&([S_{52}] + [S_{NL\_29}])\{s_t\} + ([S_{53}] + [S_{NL\_30}])\{s_r\} + ([S_{54}] + [S_{NL\_31}])\{s_{r*}\} \\
&+[S_{F26}](\{F_\psi\} - \{F_{t\psi}\}) - [S_{F25}](\{F_\phi\} - \{F_{T\phi}\}) = \{F_T\} \\
&([S_{55}] + [S_{NL\_33}])\{s_t\} + ([S_{56}] + [S_{NL\_34}])\{s_r\} \\
&+[S_{F32}](\{F_\psi\} - \{F_{T\psi}\}) - [S_{F31}](\{F_\phi\} - \{F_{T\phi}\}) = \{F_T\} \\
&[S_{eq}]\{s_t\} + [S_{NL\_eq}]\{s_t\} = \{F_{eq}\} \\
&\{s_t\} = ([S_{eq}] + [S_{NL\_eq}])^{-1}\{F_{eq}\}
\end{aligned}
\tag{A-5}
$$

Appendix B

The different stiffness matrices leading to linear equivalent stiffness matrix $[S_{L\_eq}]$ can be denoted as,

$$[S_1^e] = [S_{tb1}^e] + [S_{ts1}^e]; [S_2^e] = [S_{rtb24}^e]^T + [S_{rts13}^e]^T$$

$$[S_3^e] = [S_{rtb4}^e]^T + [S_{rts3}^e]^T; [S_4^e] = [S_{tb\phi1}^e]^T + [S_{ts\phi1}^e]^T$$

$$[S_5^e] = [S_{tb\psi1}^e]^T + [S_{ts\psi1}^e]^T; [S_6^e] = [S_{rtb24}^e] + [S_{rts13}^e]$$

$$[S_7^e] = [S_{rrb3557}^e] + [S_{rrs3513}^e]; [S_8^e] = [S_{rrb57}^e] + [S_{rrs35}^e]$$

$$[S_9^e] = [S_{rb\phi24}^e]^T + [S_{r\phi s13}^e]^T; [S_{10}^e] = [S_{rb\psi24}^e]^T + [S_{r\psi s13}^e]^T$$

$$[S_{11}^e] = [S_{rtb4}^e] + [S_{rts3}^e]; [S_{12}^e] = [S_{rrb57}^e] + [S_{rrs35}^e]$$

$$[S_{13}^e] = [S_{rrb7}^e] + [S_{rrs5}^e]; [S_{14}^e] = [S_{rb\phi4}^e]^T + [S_{r\phi s3}^e]^T$$

$$[S_{15}^e] = [S_{rb\psi4}^e]^T + [S_{r\psi s3}^e]^T; [S_{16}^e] = [S_{tb\phi1}^e]^T + [S_{ts\phi1}^e]^T$$

$$[S_{17}^e] = [S_{rb\phi2}^e]^T + [S_{rb\phi4}^e]^T + [S_{r\phi s1}^e]^T + [S_{r\phi s3}^e]^T;$$

$$[S_{18}^e] = [S_{rb\phi4}^e]^T + [S_{r\phi s3}^e]^T; [S_{19}^e] = [S_{tb\psi1}^e]^T + [S_{ts\psi1}^e]^T$$

$$[S_{20}^e] = [S_{rb\psi2}^e]^T + [S_{rb\psi4}^e]^T + [S_{r\psi s1}^e]^T + [S_{r\psi s3}^e]^T;$$

$$[S_{21}^e] = [S_{rb\psi4}^e]^T + [S_{r\psi s3}^e]^T; [S_{22}^e] = ([S_{16}] - [S_{\phi\psi}][S_{\psi\psi}]^{-1}[S_{19}])$$

$$[S_{23}^e] = [S_{17}^e] - [S_{\phi\psi}^e][S_{\psi\psi}^e]^{-1}[S_{20}^e], [S_{24}^e] = [S_{18}^e] - [S_{\phi\psi}^e][S_{\psi\psi}^e]^{-1}[S_{21}^e]$$

$$[S_{25}^e] = [S_{\phi\phi}^e] - [S_{\phi\psi}^e][S_{\psi\psi}^e]^{-1}[S_{\phi\psi}^e]^T$$

$$[S_{26}^e] = [S_{25}^e]^{-1}[S_{22}^e]^T; [S_{27}^e] = [S_{25}^e]^{-1}[S_{23}^e]^T; [S_{28}^e] = [S_{25}^e]^{-1}[S_{24}^e]^T \quad \text{(B-1)}$$

$$[S_{29}^e] = [S_{11}^e] - [S_{15}^e][S_{\psi\psi}^e]^{-1}[S_{19}^e]; [S_{30}^e] = [S_{12}^e] - [S_{15}^e][S_{\psi\psi}^e]^{-1}[S_{20}^e]$$

$$[S_{31}^e] = [S_{13}^e] - [S_{15}^e][S_{\psi\psi}^e]^{-1}[S_{21}^e]; [S_{32}^e] = [S_{14}^e] - [S_{15}^e][S_{\psi\psi}^e]^{-1}[S_{\phi\psi}^e]^T$$

$$[S_{33}^e] = [S_{29}^e] - [S_{32}^e][S_{26}^e], [S_{34}^e] = [S_{30}^e] - [S_{32}^e][S_{27}^e]$$

$$[S_{35}^e] = [S_{31}^e] - [S_{32}^e][S_{28}^e]; [S_{36}^e] = [S_{35}^e]^{-1}[S_{33}^e]^T;$$

$$[S_{37}^e] = [S_{35}^e]^{-1}[S_{34}^e]^T; [S_{38}^e] = [S_6^e] - [S_{10}^e][S_{\psi\psi}^e]^{-1}[S_{19}^e];$$

$$[S_{39}^e] = [S_7^e] - [S_{10}^e][S_{\psi\psi}^e]^{-1}[S_{20}^e]; [S_{40}^e] = [S_8^e] - [S_{10}^e][S_{\psi\psi}^e]^{-1}[S_{21}^e];$$

$$[S_{41}^e] = [S_9^e] - [S_{10}^e][S_{\psi\psi}^e]^{-1}[S_{\phi\psi}^e]^T; [S_{42}^e] = [S_{38}^e] - [S_{41}^e][S_{26}^e]$$

$$[S_{43}^e] = [S_{39}^e] - [S_{41}^e][S_{27}^e]; [S_{44}^e] = [S_{40}^e] - [S_{41}^e][S_{28}^e]$$

$$[S_{45}^e] = [S_{42}^e] - [S_{44}^e][S_{36}^e]; [S_{46}^e] = [S_{43}^e] - [S_{44}^e][S_{37}^e]$$

$$[S_{47}^e] = [S_{46}^e]^{-1}[S_{45}^e]; [S_{48}^e] = [S_1^e] - [S_5^e][S_{\psi\psi}^e]^{-1}[S_{19}^e]$$

$$[S_{49}^e] = [S_2^e] - [S_5^e][S_{\psi\psi}^e]^{-1}[S_{20}^e]; [S_{50}^e] = [S_3^e] - [S_5^e][S_{\psi\psi}^e]^{-1}[S_{21}^e]$$

$$[S_{51}^e] = [S_4^e] - [S_5^e][S_{\psi\psi}^e]^{-1}[S_{\phi\psi}^e]^T; [S_{52}^e] = [S_{48}^e] - [S_{51}^e][S_{26}^e]$$

$$[S_{53}^e] = [S_{49}^e] - [S_{51}^e][S_{27}^e]; [S_{54}^e] = [S_{50}^e] - [S_{51}^e][S_{28}^e]$$

$$[S_{55}^e] = [S_{52}^e] - [S_{54}^e][S_{36}^e]; [S_{56}^e] = [S_{53}^e] - [S_{54}^e][S_{37}^e]$$

$$[S_{L\_eq}^e] = [S_{55}^e] - [S_{56}^e][S_{47}^e]$$

Similarly, the matrices giving rise to the equivalent nonlinear stiffness matrix $[S_{NL\_eq}]$ can be written as follows:

$$[S_{NL\_1}^e] = [S_{tbNLbNL1\_tbtbNL1}^e]; [S_{NL\_2}^e] = [S_{rbNL\_rtb24}^e]^T$$

$$[S_{NL\_3}^e] = [S_{rbNL4}^e]^T; [S_{NL\_4}^e] = [S_{bNL\phi1}^e]$$

$$[S_{NL\_5}^e] = [S_{bNL\psi1}^e]; [S_{NL\_6}^e] = [S_{rbNL24}^e]^T$$

$$[S_{NL\_7}^e] = [S_{rbNL4}^e]^T; [S_{NL\_8}^e] = [S_{bNL\phi1}^e]^T; [S_{NL\_9}^e] = [S_{bNL\psi1}^e]^T$$

$$[S_{NL\_10}^e] = [S_{\phi\psi}^e][S_{\psi\psi}^e]^{-1}[S_{NL\_9}^e], [S_{NL\_11}^e] = [S_{NL\_8}^e] - [S_{NL\_10}^e]$$

$$[S_{NL\_12}^e] = [S_{25}^e]^{-1}[S_{NL\_11}^e]; [S_{NL\_13}^e] = [S_{NL\_7}^e] - [S_{15}^e][S_{\psi\psi}^e]^{-1}[S_{NL\_9}^e];$$

$$[S_{NL\_14}^e] = [S_{32}^e][S_{NL\_12}^e]; [S_{NL\_15}^e] = [S_{NL\_14}^e] - [S_{NL\_13}^e];$$

$$[S_{NL\_16}^e] = [S_{35}^e]^{-1}[S_{NL\_15}^e]; [S_{NL\_17}^e] = [S_{10}^e][S_{\psi\psi}^e]^{-1}[S_{NL\_9}^e];$$

$$[S_{NL\_18}^e] = [S_{NL\_6}^e] - [S_{NL\_17}^e]; [S_{NL\_19}^e] = [S_{41}^e][S_{NL\_12}^e];$$

$$[S_{NL\_20}^e] = [S_{NL\_19}^e] - [S_{NL\_18}^e]; [S_{NL\_21}^e] = [S_{44}^e][S_{NL\_16}^e];$$

$$[S_{NL\_22}^e] = [S_{NL\_20}^e] - [S_{NL\_21}^e]; [S_{NL\_23}^e] = [S_{46}^e]^{-1}[S_{NL\_22}^e];$$

$$[S_{NL\_24}^e] = \begin{pmatrix} [S_{NL\_1}^e] - [S_{NL\_5}^e][S_{\psi\psi}^e]^{-1}[S_{19}^e] - [S_5^e][S_{\psi\psi}^e]^{-1}[S_{NL\_9}^e] \\ -[S_{NL\_5}^e][S_{\psi\psi}^e]^{-1}[S_{NL\_9}^e] \end{pmatrix}$$

$$[S_{NL\_25}^e] = [S_{NL\_2}^e] - [S_{NL\_5}^e][S_{\psi\psi}^e]^{-1}[S_{20}^e]$$

$$[S_{NL\_26}^e] = [S_{NL\_3}^e] - [S_{NL\_5}^e][S_{\psi\psi}^e]^{-1}[S_{21}^e]$$

$$[S_{NL\_27}^e] = [S_{NL\_4}^e] - [S_{NL\_5}^e][S_{\psi\psi}^e]^{-1}[S_{\psi\phi}^e]$$

$$[S_{NL\_28}^e] = [S_{51}^e][S_{NL\_12}^e]$$

$$[S_{NL\_29}^e] = -[S_{NL\_28}^e] + [S_{NL\_24}^e] - [S_{NL\_27}^e][S_{26}^e] - [S_{NL\_27}^e][S_{NL\_12}^e]$$

$$[S_{NL\_30}^e] = [S_{NL\_25}^e] - [S_{NL\_27}^e][S_{27}^e], [S_{NL\_31}^e] = [S_{NL\_26}^e] - [S_{NL\_27}^e][S_{28}^e];$$

$$[S_{NL\_32}^e] = [S_{54}^e][S_{NL\_16}^e];$$

$$[S_{NL\_33}^e] = [S_{NL\_29}^e] - [S_{NL\_32}^e] - [S_{NL\_31}^e][S_{36}^e] - [S_{NL\_31}^e][S_{NL\_16}^e]$$

$$[S_{NL\_34}^e] = [S_{NL\_30}^e] - [S_{NL\_31}^e][S_{37}^e]$$

$$[S_{NL\_35}^e] = [S_{56}^e][S_{NL\_23}^e], [S_{NL\_36}^e] = [S_{NL\_34}^e][S_{47}^e]$$

$$[S_{NL\_37}^e] = [S_{NL\_34}^e][S_{NL\_23}^e]$$

$$[S_{NL\_eq}^e] = [S_{NL\_33}^e] - [S_{NL\_35}^e] - [S_{NL\_36}^e] - [S_{NL\_37}^e]$$

The matrices contributing to the equivalent force $\{F_{eq}\}$ are,

$$\{F_{eq}\} = \{F_T\} - \left[S^e_{F\phi}\right]\left(\{F_\phi\} + \{F_{T\phi}\}\right) - \left[S^e_{F\psi}\right]\left(\{F_\psi\} + \{F_{T\psi}\}\right) \tag{B-2}$$

where

$$\left[S^e_{F\phi}\right] = \left[S^e_{F31}\right] - \left[S^e_{F35}\right] - \left[S^e_{F33}\right]; \left[S^e_{F\psi}\right] = \left[S^e_{F32}\right] - \left[S^e_{F36}\right] - \left[S^e_{F34}\right]$$

$$\left[S^e_{F1}\right] = \left[S^e_{25}\right]^{-1}\left[S^e_{\phi\psi}\right]\left[S^e_{\psi\psi}\right]^{-1}; \left[S^e_{F2}\right] = \left[S^e_{15}\right]\left[S^e_{\psi\psi}\right]^{-1}$$

$$\left[S^e_{F3}\right] = \left[S^e_{32}\right]\left[S^e_{25}\right]^{-1}; \left[S^e_{F4}\right] = \left[S^e_{32}\right]\left[S^e_{F1}\right]$$

$$\left[S^e_{F5}\right] = \left[S^e_{F2}\right] - \left[S^e_{F4}\right]; \left[S^e_{F6}\right] = \left[S^e_{35}\right]^{-1}\left[S^e_{F5}\right]$$

$$\left[S^e_{F7}\right] = \left[S^e_{35}\right]^{-1}\left[S^e_{F3}\right]; \left[S^e_{F8}\right] = \left[S^e_{10}\right]\left[S^e_{\psi\psi}\right]^{-1}$$

$$\left[S^e_{F9}\right] = \left[S^e_{41}\right]\left[S^e_{F1}\right]; \left[S^e_{F10}\right] = \left[S^e_{41}\right]\left[S^e_{25}\right]^{-1}; \left[S^e_{F11}\right] = \left[S^e_{F8}\right] - \left[S^e_{F9}\right]$$

$$\left[S^e_{F12}\right] = \left[S^e_{44}\right]\left[S^e_{F6}\right];$$

$$\left[S^e_{F13}\right] = \left[S^e_{44}\right]\left[S^e_{F7}\right]; \left[S^e_{F14}\right] = \left[S^e_{F10}\right] - \left[S^e_{F13}\right]$$

$$\left[S^e_{F15}\right] = \left[S^e_{F11}\right] - \left[S^e_{F12}\right]; \left[S^e_{F16}\right] = \left[S^e_{46}\right]^{-1}\left[S^e_{F14}\right];$$

$$\left[S^e_{F17}\right] = \left[S^e_{46}\right]^{-1}\left[S^e_{F15}\right]; \left[S^e_{F18}\right] = \left[S^e_{5}\right]\left[S^e_{\psi\psi}\right]^{-1} \tag{B-3}$$

$$\left[S^e_{F19}\right] = \left[S^e_{NL\_5}\right]\left[S^e_{\psi\psi}\right]^{-1}; \left[S^e_{F20}\right] = \left[S^e_{F18}\right] + \left[S^e_{F19}\right]$$

$$\left[S^e_{F21}\right] = \left[S^e_{51}\right]\left[S^e_{F1}\right]; \left[S^e_{F22}\right] = \left[S^e_{51}\right]\left[S^e_{25}\right]^{-1}$$

$$\left[S^e_{F23}\right] = \left[S^e_{NL\_27}\right]\left[S^e_{F1}\right]; \left[S^e_{F24}\right] = \left[S^e_{NL\_27}\right]\left[S^e_{25}\right]^{-1}$$

$$\left[S^e_{F25}\right] = \left[S^e_{F22}\right] + \left[S^e_{F24}\right]; \left[S^e_{F26}\right] = \left[S^e_{F20}\right] - \left[S^e_{F21}\right] - \left[S^e_{F23}\right]$$

$$\left[S^e_{F27}\right] = \left[S^e_{54}\right]\left[S^e_{F6}\right]; \left[S^e_{F28}\right] = \left[S^e_{54}\right]\left[S^e_{F7}\right]$$

$$\left[S^e_{F29}\right] = \left[S^e_{NL\_31}\right]\left[S^e_{F6}\right]; \left[S^e_{F30}\right] = \left[S^e_{NL\_31}\right]\left[S^e_{F7}\right]$$

$$\left[S^e_{F31}\right] = \left[S^e_{F25}\right] + \left[S^e_{F30}\right] + \left[S^e_{F28}\right]; \left[S^e_{F32}\right] = \left[S^e_{F26}\right] - \left[S^e_{F29}\right] - \left[S^e_{F27}\right]$$

$$\left[S^e_{F33}\right] = \left[S^e_{56}\right]\left[S^e_{F16}\right]; \left[S^e_{F34}\right] = \left[S^e_{56}\right]\left[S^e_{F17}\right]; \left[S^e_{F35}\right] = \left[S^e_{NL\_34}\right]\left[S^e_{F16}\right];$$

$$\left[S^e_{F36}\right] = \left[S^e_{NL\_34}\right]\left[S^e_{F17}\right]$$

$$\left[S^e_{F37}\right] = \left[S^e_{F32}\right] - \left[S^e_{F34}\right] - \left[S^e_{F36}\right]$$

$$\left[S^e_{F38}\right] = \left[S^e_{F33}\right] + \left[S^e_{F35}\right] - \left[S^e_{F31}\right]$$

$$\left[S^e_{rrs35}\right] = \left[S^e_{rrs3}\right] + \left[S^e_{rrs5}\right], \left[S^e_{rrs13}\right] = \left[S^e_{rrs1}\right] + \left[S^e_{rrs3}\right]$$

$$\left[S^e_{rrs3513}\right] = \left[S^e_{rrs35}\right] + \left[S^e_{rrs13}\right], \left[S^e_{rts13}\right] = \left[S^e_{rts1}\right] + \left[S^e_{rts3}\right]$$

$$\left[S^e_{r\psi s13}\right] = \left[S^e_{r\psi s1}\right] + \left[S^e_{r\psi s3}\right], \left[S^e_{r\phi s13}\right] = \left[S^e_{r\phi s1}\right] + \left[S^e_{r\phi s3}\right]$$

$$\left[S^e_{tbtbNL1}\right] = \left[S^e_{tb1}\right] + \left[S^e_{tbNL1}\right], \left[S^e_{rtb24}\right] = \left[S^e_{rtb2}\right] + \left[S^e_{rtb4}\right]$$

$$\left[S^e_{tbNLbNL1\_tbtbNL1}\right] = \left[S^e_{tbNLbNL1}\right] + \left[S^e_{tbtbNL1}\right],$$

$$\left[S^e_{rbNL\_rtb24}\right] = \left[S^e_{rbNL24}\right] + \left[S^e_{rtb24}\right], \left[S^e_{rbNL\_rtb4}\right] = \left[S^e_{rbNL4}\right] + \left[S^e_{rtb4}\right] \tag{B-4}$$

$$\left[S^e_{bNL\_tb\phi1}\right] = \left[S^e_{bNL\phi1}\right] + \left[S^e_{tb\phi1}\right], \left[S^e_{bNL\_tb\psi1}\right] = \left[S^e_{bNL\psi1}\right] + \left[S^e_{tb\psi1}\right]$$

$$\left[S^e_{rrb57}\right] = \left[S^e_{rrb5}\right] + \left[S^e_{rrb7}\right], \left[S^e_{rtbrbNL4}\right] = \left[S^e_{rtb4}\right] + \left[S^e_{rbNL4}\right]$$

$$\left[S^e_{rtbrbNL2}\right] = \left[S^e_{rtb2}\right] + \left[S^e_{rbNL2}\right], \left[S^e_{rtbrbNL24}\right] = \left[S^e_{rtbrbNL2}\right] + \left[S^e_{rtbrbNL4}\right]$$

$$\left[S^e_{rrb35}\right] = \left[S^e_{rrb3}\right] + \left[S^e_{rrb5}\right], \left[S^e_{rrb5735}\right] = \left[S^e_{rrb57}\right] + \left[S^e_{rrb35}\right]$$

$$\left[S^e_{rb\phi24}\right] = \left[S^e_{rb\phi2}\right] + \left[S^e_{rb\phi4}\right], \left[S^e_{rb\psi24}\right] = \left[S^e_{rb\psi2}\right] + \left[S^e_{rb\psi4}\right]$$

$$\left[S^e_{tbNLbNL1}\right] = \left[S^e_{tbNL1}\right] + \left[S^e_{bNL1}\right], \left[S^e_{rbNL24}\right] = \left[S^e_{rbNL2}\right] + \left[S^e_{rbNL4}\right]$$

where

$$[S^e_{rtb4}] = \int_0^a\int_0^b [SD_{rb}]^T[D_{b4}][SD_{tb}] \ dxdy; \ [S^e_{rbNL4}] = \int_0^a\int_0^b [SD_{rb}]^T[D_{bNL4}][SD_1] \ [SD_2] \ dxdy$$

$$[S^e_{rrb5}] = \int_0^a\int_0^b [SD_{rb}]^T[D_{b5}][SD_{rb}] \ dxdy; \ [S^e_{rrb7}] = \int_0^a\int_0^b [SD_{rb}]^T[D_{b7}][SD_{rb}] \ dxdy$$

$$[S^e_{rb\phi4}] = \int_0^a\int_0^b [SD_{rb}]^T[D_{b\phi4}][SD_\phi] \ dxdy; \ [S^e_{rb\psi4}] = \int_0^a\int_0^b [SD_{rb}]^T[D_{b\psi4}][SD_\psi] \ dxdy$$

$$[S^e_{rtb4}] = \int_0^a\int_0^b [SD_{rb}]^T[D_{b4}][SD_{tb}] \ dxdy; \ [S^e_{rtb2}] = \int_0^a\int_0^b [SD_{rb}]^T[D_{b2}][SD_{tb}] \ dxdy$$

$$[S^e_{rbNL2}] = \int_0^a\int_0^b [SD_{rb}]^T[D_{bNL2}][SD_1] \ [SD_2] \ dxdy; \ [S^e_{rrb3}] = \int_0^a\int_0^b [SD_{rb}]^T[D_{b3}][SD_{rb}] \ dxdy$$

$$[S^e_{rrb5}] = \int_0^a\int_0^b [SD_{rb}]^T[D_{b5}][SD_{rb}] \ dxdy; \ [S^e_{rb\phi2}] = \int_0^a\int_0^b [SD_{rb}]^T[D_{b\phi2}][SD_\phi] \ dxdy$$

$$[S^e_{rb\psi2}] = \int_0^a\int_0^b [SD_{rb}]^T[D_{b\psi2}][SD_\psi] \ dxdy; \ [S^e_{tbNL1}] = \int_0^a\int_0^b [SD_{tb}]^T[D_{bNL1}][SD_1] \ [SD_2] \ dxdy$$

$$[S^e_{bNL1}] = \int_0^a\int_0^b [SD_2]^{\ T}[SD_1]^{\ T}[D_{bbNL1}][SD_1] \ [SD_2] \ dxdy;$$

$$[S^e_{bNL\phi1}] = \int_0^a\int_0^b [SD_\phi]^T[D_{bNL\phi1}][SD_1] \ [SD_2] \ dxdy; \ [S^e_{bNL\psi1}] = \int_0^a\int_0^b [SD_\psi]^T[D_{bNL\psi1}][SD_1] \ [SD_2] \ dxdy$$

$$[S^e_{tb1}] = \int_0^a\int_0^b [SD_{tb}]^T[D_{b1}][SD_{tb}] \ dxdy; \ [S^e_{tb\phi1}] = \int_0^a\int_0^b [SD_{tb}]^T[D_{b\phi1}][SD_\phi] \ dxdy \qquad \text{(B-5)}$$

$$[S^e_{tb\psi1}] = \int_0^a\int_0^b [SD_{tb}]^T[D_{b\psi1}][SD_\psi] \ dxdy; \ [S^e_{rts3}] = \int_0^a\int_0^b [SD_{rs}]^T[D_{s3}][SD_{ts}] \ dxdy$$

$$[S_{rrs3}] = \int_0^a\int_0^b [SD_{rs}]^T[D_{s3}][SD_{rs}] \ dxdy; \ [S^e_{rrs5}] = \int_0^a\int_0^b [SD_{rs}]^T[D_{s5}][SD_{rs}] \ dxdy$$

$$[S_{r\psi s3}] = \int_0^a\int_0^b [SD_{rs}]^T[D_{s\psi3}][SD_\psi] \ dxdy; \ [S^e_{r\phi s3}] = \int_0^a\int_0^b [SD_{rs}]^T[D_{s\phi3}][SD_\phi] \ dxdy$$

$$[S^e_{ts\phi1}] = \int_0^a\int_0^b [SD_{ts}]^T[D_{s\phi1}][SD_\phi] \ dxdy; \ [S^e_{ts\psi1}] = \int_0^a\int_0^b [SD_{ts}]^T[D_{s\psi1}][SD_\psi] \ dxdy$$

$$[S^e_{r\phi s1}] = \int_0^a\int_0^b [SD_{rs}]^T[D_{s\phi1}][SD_\phi] \ dxdy; \ [S_{r\psi s1}] = \int_0^a\int_0^b [SD_{rs}]^T[D_{s\psi1}][SD_\psi] \ dxdy$$

$$[S^e_{rts1}] = \int_0^a\int_0^b [SD_{rs}]^T[D_{s1}][SD_{ts}] \ dxdy; \ [S^e_{rrs1}] = \int_0^a\int_0^b [SD_{rs}]^T[D_{s1}][SD_{rs}] \ dxdy$$

$$[S_{ts1}] = \int_0^a\int_0^b [SD_{ts}]^T[D_{s1}][SD_{ts}] \ dxdy; \ [S^e_{rts3}] = \int_0^a\int_0^b [SD_{rs}]^T[D_{s3}][SD_{ts}] \ dxdy$$

$$\{F_\psi\} = \int_0^a\int_0^b [N_\psi]^T Q^\psi \ dxdy; \ \{F_\phi\} = \int_0^a\int_0^b [N_\phi]^T Q^\phi \ dxdy;$$

$$\{F_t\} = \int_{\Omega^N} [C_b]^N [\alpha]^N \Delta T d\Omega^N; \ \{F_{t\phi}\} = \int_{\Omega^N} [p]\Delta T d\Omega^N; \ \{F_{t\psi}\} = \int_{\Omega^N} [\tau]\Delta T d\Omega^N;$$

The rigidity matrices appearing in Eq. (B-5) can be written as follows:

$$[D_{b1}] = \sum_{N=1}^{3} \int_{-h/2}^{h/2} [C_b]^N \, dz; \ [D_{bbNL1}] = \frac{1}{4}[D_{b1}]; \ [D_{bNL1}] = \frac{1}{2}[D_{b1}];$$

$$[D_{b2}] = \sum_{N=1}^{3} \int_{-h/2}^{h/2} z[C_b]^N \, dz; \ [D_{bNL2}] = \frac{1}{2}[D_{b2}]; \ [D_{b3}] = \sum_{N=1}^{3} \int_{-h/2}^{h/2} z^2 [C_b]^N dz;$$

$$[D_{b4}] = \sum_{N=1}^{3} \int_{-h/2}^{h/2} c_1 z^3 [C_b]^N dz; \ [D_{bNL4}] = \frac{1}{2}[D_{b4}]; \ [D_{b5}] = \sum_{N=1}^{3} \int_{-h/2}^{h/2} c_1 z^4 [C_b]^N dz;$$

$$[D_{b7}] = \sum_{N=1}^{3} \int_{-h/2}^{h/2} c_1^2 z^6 [C_b]^N dz; \ [D_{b\phi1}] = \int_{h_3}^{h_4} [Z_t][e_b] dz + \int_{h_1}^{h_2} [Z_b][e_b] dz;$$

$$[D_{bNL\phi1}] = [D_{b\phi1}]; \ [D_{b\phi2}] = \int_{h_3}^{h_4} z[Z_t][e_b] dz + \int_{h_1}^{h_2} z[Z_b][e_b] dz;$$

$$[D_{b\phi4}] = \int_{h_3}^{h_4} c_1 z^3 [Z_t][e_b] dz + \int_{h_1}^{h_2} c_1 z^3 [Z_b][e_b] dz; \ [D_{s1}] = \sum_{N=1}^{3} \int_{-h/2}^{h/2} [C_s]^N dz;$$

$$[D_{b\psi1}] = \int_{h_3}^{h_4} [Z_t][q_b] dz + \int_{h_1}^{h_2} [Z_b][q_b] dz; \ [D_{bNL\psi1}] = [D_{b\psi1}]$$

$$[D_{b\psi2}] = \int_{h_3}^{h_4} z[Z_t][q_b] dz + \int_{h_1}^{h_2} z[Z_b][q_b] dz; \tag{B-6}$$

$$[D_{b\psi4}] = \int_{h_3}^{h_4} c_1 z^3 [Z_t][q_b] dz + \int_{h_1}^{h_2} c_1 z^3 [Z_b][q_b] dz; \ [D_{s3}] = \sum_{N=1}^{3} \int_{-h/2}^{h/2} c_2 z^2 [C_s]^N \, dz;$$

$$[D_{s5}] = \sum_{N=1}^{3} \int_{-h/2}^{h/2} c_2^2 z^4 [C_s]^N dz; \ [D_{s\phi1}] = \int_{h_3}^{h_4} [Z_t][e_s]^T dz + \int_{h_1}^{h_2} [Z_b][e_s]^T dz;$$

$$[D_{s\phi3}] = \int_{h_3}^{h_4} c_2 z^2 [Z_t][e_s]^T dz + \int_{h_1}^{h_2} c_2 z^2 [Z_b][e_s]^T dz;$$

$$[D_{s\psi1}] = \int_{h_3}^{h_4} [Z_t][q_s]^T dz + \int_{h_1}^{h_2} [Z_b][q_s]^T dz;$$

$$[D_{s\psi3}] = \int_{h_3}^{h_4} c_2 z^2 [Z_t][q_s]^T dz + \int_{h_1}^{h_2} c_2 z^2 [Z_b][q_s]^T dz;$$

$$[D_{\phi\phi}] = \int_{h_3}^{h_4} [Z_t]^T [\eta][Z_t] dz + \int_{h_1}^{h_2} [Z_b]^T [\eta][Z_b] dz; \ [D_{\psi\psi}] = \int_{h_3}^{h_4} [Z_t]^T [\mu][Z_t] dz + \int_{h_1}^{h_2} [Z_b]^T [\mu][Z_b] dz;$$

$$[D_{\phi\psi}] = \int_{h_3}^{h_4} [Z_t]^T [m][Z_t] dz + \int_{h_1}^{h_2} [Z_b]^T [m][Z_b] dz;$$

The derivative of shape function matrices appearing in the FE formulation can be represented by

$$[SD_{tb}] = \begin{bmatrix} N_{i,x} & 0 & 0 \\ 0 & N_{i,y} & 0 \\ N_{i,y} & N_{i,x} & 0 \end{bmatrix}, \ [SD_{rb}] = \begin{bmatrix} N_{i,x} & 0 \\ 0 & N_{i,y} \\ N_{i,y} & N_{i,x} \end{bmatrix}, \ [SD_{ts}] = \begin{bmatrix} 0 & 0 & N_{i,x} \\ 0 & 0 & N_{i,y} \end{bmatrix}, \ [SD_{rs}] = \begin{bmatrix} 1 & 0 \\ 0 & 1 \end{bmatrix}$$

$$[SD_1] = \begin{bmatrix} w_{0,x} & 0 & w_{0,y} \\ 0 & w_{0,y} & w_{0,x} \end{bmatrix}^T, \ [B_2] = \begin{bmatrix} SD_{21} & SD_{22} & \cdots & SD_{28} \end{bmatrix}; \ [SD_\phi] = [SD_\psi] = \begin{bmatrix} N_{i,x} \\ N_{i,y} \\ N_{i,z} \end{bmatrix} \tag{B-7}$$